Universidade de Aveiro Departamento de Física,
2017

Ema Filipa dos Santos Valente

Um modelo simples de objetos compactos exóticos: interação com um campo escalar

A simple model of exotic compact objects: interaction with a scalar field

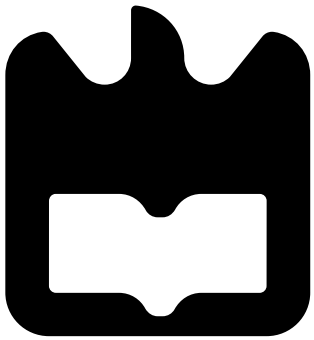

Ema Filipa dos Santos Valente

Um modelo simples de objetos compactos exóticos: interação com um campo escalar

A simple model of exotic compact objects: interaction with a scalar field

Dissertação apresentada à Universidade de Aveiro para cumprimento dos requesitos necessários à obtenção do grau de Mestre em Mestrado em Física, realizada sob a orientação científica do Prof. Dr. Carlos Alberto Ruivo Herdeiro, Investigador Principal do Departamento de Física da Universidade de Aveiro

o júri / the jury

presidente / president

Manuel António dos Santos Barroso
Professor Auxiliar do Departamento de Física da Universidade de Aveiro

vogais / examiners committee

Luís Carlos Bassalo Crispino
Professor Catedrático da Universidade Federal do Pará (UFPa), Brasil (examinador)

Carlos Alberto Ruivo Herdeiro
Professor Auxiliar com Agregação, equiparado a investigador principal do Departamento de Física da Universidade de Aveiro (orientador)

Agradecimentos / Acknowledgements

Queria agradecer ao professor doutor Carlos Herdeiro por me propor um projeto bastante interessante para a dissertação de Mestrado; pela sua disponibilidade e paciência ao longo do projeto.

A nível pessoal, queria agradecer ao Alexandre por estar sempre a apoiar-me mesmo quando sou teimosa, fazendo-me feliz todos os dias com muito amor e carinho. À minha mãe que, apesar de estar longe, sempre me apoiou moralmente e nas minhas decisões ao longo da vida. E ao resto da minha família por me apoiarem desde sempre.

Por último, quero agradecer ao meu pai, que apesar de não estar presente, sempre me apoiou nos meus sonhos, dedicando-lhe, assim, esta tese.

Resumo

Modelos de objetos compactos exóticos (OCEs) foram propostos nas últimas décadas como alternativas aos buracos negros. Esses modelos visam reproduzir a fenomenologia que caracteriza os (candidatos a) buracos negros observados. No entanto, para superar os problemas associados ao horizonte de eventos (e à consequente singularidade de curvatura, de acordo com o teorema de Penrose), estes OCEs não possuem horizonte de eventos.

Nesta dissertação, exploramos um modelo simples de um OCE, descrito pela métrica de Kerr-Newman no exterior de uma superfície com condições de fronteira reflectivas, localizada fora do horizonte de eventos de Kerr-Newman. Nesta geometria, estudamos OCEs que podem estar em equilíbrio com configurações estáticas de um campo escalar. Consideramos um campo escalar sem massa, tanto no caso eletricamente não carregado como no caso carregado, e obtemos, através de métodos analíticos, um conjunto discreto de raios críticos da superfície do OCE que podem suportar configurações estáticas não triviais do campo escalar. Dentro deste conjunto discreto, o OCE com maior raio crítico separa os OCEs estáveis e instáveis relativamente à instabilidade superradiante, induzida por um campo escalar.

O conjunto discreto de raios críticos da superfície do OCE foi construído para os três regimes diferentes da métrica de Kerr-Newman: regime sub-extremo, regime extremo e regime super-extremo. Estes espectros de ressonância dependem dos parâmetros físicos $\{a, Q, q, l, m\}$.

Abstract

Models of exotic compact objects (ECOs) have been proposed in the past decades as alternatives to black holes. These models aim at reproducing the phenomenology that characterises the observed black hole (candidates). However, to overcome the problems associated to the event horizon (and the consequent curvature singularity, following from Penrose's singularity theorem), these ECOs do not possess an event horizon.

In this thesis, we explore a simple ECO model, described by the Kerr-Newman metric in the exterior of a surface wherein reflective boundary conditions are imposed, placed outside the event horizon of the Kerr-Newman geometry. We then study, on this geometry, ECOs that may be in equilibrium with static scalar field configurations. We consider both electrically charged and uncharged massless scalar fields, and, using analytical methods, we obtain a discrete set of critical ECO surface radii that can support static scalar field configurations. Within this discrete set, the ECO with the largest critical surface radius separates stable and unstable Kerr-Newman-type ECOs against the superradiant instability induced by a scalar field.

The discrete set of ECO critical surface radii was constructed for three different regimes of the Kerr-Newman metric: sub-extremal regime, extremal regime and super-extremal regime. These resonance spectra are dependent on the physical parameters $\{a, Q, q, l, m\}$.

Contents

List of Figures

List of Tables

Chapter 1

Introduction

Black holes (BHs) are perhaps the most mysterious and intriguing objects that exist in our universe. Being a prediction of Einstein's general relativity, BHs are theoretically characterized by curved spacetimes geometries with a peculiar structure. For the paradigmatic BHs of classical general relativity, this structure includes a curvature singularity at the BH "core", cloacked by an all absorbing boundary, denominated *event horizon*.

BH physics has been an extensively investigated research area over more than half a century. Some of this research unveiled difficult technical and conceptual issues that arise for these compact objects, in particular, due to the presence of the event horizon and singularity. The latter hints at a breakdown of the classical description provided by general relativity. To overcome these paradoxes, some researchers proposed models of *exotic compact objects* (ECOs) as alternatives to BHs. The idea is that these objects mimic BH phenomenology currently observed, thus being compatible with observations, but they have no horizon or singularity, being thus free of the associated problems. Example of ECOs include boson stars, fuzzballs, gravastars or wormholes.

The current astrophysical observations seem, however, to be compatible with the Kerr metric, at least within the current precision. But it is also true that current observations do not really probe the Kerr metric all the way up to the event horizon. Thus, it seems reasonable to consider an ECO which only differs from the Kerr geometry close to the horizon. With this motivation, we shall, in this dissertation, consider a simple ECO model, characterized by the Kerr-Newman metric up to the vicinity of the (would-be) horizon. Instead of having a horizon, however, the ECO has a surface wherein reflective boundary conditions are imposed. By following the works of [1–3] we study the ECO's (in)stability when subjected to scalar field perturbations obtaining a set of critical surface radii for the ECO that can be in equilibrium with a static scalar field non-trivial configuration.

This dissertation is organised as follows. In chapter 2 we introduce the concept of BHs. We start with an overview of some historical aspects and features of BHs, proceeding to the description of the Kerr-Newman spacetime, some physical properties and the uniqueness theorems. We also describe the Kerr-Newman spacetime subject to a massive and charged scalar field perturbation and discuss its properties. In Chapter 3 we introduce the ECOs and review a recent no-hair theorem for spherically symmetric ECOs subjected to a real scalar field, proved in [4]. In addition we study the possibility to establish this theorem for the same system, however subjected to a complex scalar field with a harmonic time dependence. In Chapters 4 and 5 we explore a unique family of critical (marginally-stable) Kerr-Newman-like ECOs for an uncharged and charged massless scalar field, respectively. We construct a discrete set of critical surface radii, characterized by reflective boundary conditions, that allow equilibrium with a static scalar field, for three different regimes: the sub-extremal regime, the extremal regime and the super-extremal regime. In addition, we explore the extremal Kerr-type ECO which has not been, to the best of our knowledge, discussed in the literature. At last, in Chapter 6, we conclude our study. The results in this work were obtained by a simple find root routine on the compact resonances equations carried out in MATHEMATICA 11 to machine precision.

Chapter 2

Black Holes

2.1 Overview

Speculations of a massive body that even light could not escape from, were first considered in the 18th century by the British clergyman and natural philoshoper John Michell [5]. Accepting Newton's corpuscular theory of light (where light is made of particles), he argued that due to the star's gravitational pull, these radiated particles could be slowed down, and based on their speed reduction, it was possible to calculate the mass of the star. With that idea in mind, he though of an extreme case where the star's gravity was so strong that the escape velocity would exceed the speed of light. The Newtonian computation, based on energy conservation, shows that when the escape velocity equals precisely the speed of light c, the mass M and radius R of the (spherical) star are related by

$$R = \frac{2GM}{c^2}, \tag{2.1}$$

where G is the Gravitational constant.

This was a Newtonian version of a "Black Hole" (BH). However, this reasoning was based on what we now know to be a misconception: the speed of light is always constant in space, independently of the local strength of gravity. Within the general theory of relativity, formulated by Einstein in 1915 [6], which describes the gravitational field when velocities are comparable to the speed of light and the gravitational field may be "strong", the modern (relativistic) version of BHs starts to emerge. In 1916, Karl Schwarzschild found a solution to the Einstein field equations [7], describing a spherical warped spacetime surrounding a concentrated mass and invisible to an outside observer. This was the beginning of BH physics. Throughout the years, many researchers contributed not only to the understanding of this solution, but also to the discovery and study of other types of BH solutions.

A natural question is if we can observe such exotic objects in the universe. Although we cannot see BHs directly, it is possible to infer their existence through indirect methods that rely on the increasingly sophisticated astronomical technology. An example is through X-rays [8]. BHs have an accretion disk that is formed due to the gravitational pull on the surrounding matter, and when the gas molecules in the disk swirl very fast, they heat up and emit X-rays. This is the case if the BH is in a binary system, and it pulls the gas from its companion star. Another detection channel is through the observation of gravitational waves arising from the coalescence of a pair of BHs. This was famously recently detected by the LIGO experiment [9–12], proving the existence of gravitational waves and providing strong evidence for the existence of stellar mass BHs in binary systems and with masses larger than those inferred from X-ray observations.

Theoretically, a BH is a geometrically defined region of spacetime that shows strong gravitational effects, and from which nothing can escape. According to the standard paradigm, the formation of BHs occurs at the final stage of the life of stars, whose 'fuel' ran out and start shrinking due to unbalanced gravity forces (gravitational collapse). For this to occur, the star has to be sufficiently massive so that no (known) nuclear physics force can prevent the gravitational collapse.

BHs can be classified as [13]:

i) *stellar-mass BHs*; from X-ray observations these have masses in the range $M \sim 3 - 30 M_\odot$ (where $M_\odot$ stands for one solar mass, $\sim 2 \times 10^{30}$ kg), but from the LIGO observations we now know these can extend to about $70 M_\odot$;

ii) *supermassive BHs*; these have masses in the range $M \sim 10^5 - 10^9 M_\odot$ and can be found in the center of galaxies;

iii) *intermediate BHs*; these have masses in the range $M \sim 10^3 M_\odot$, but are an hypothetical class whose existence is under debate;

iv) *primordial or micro-BHs*; BHs which were formed in the early universe from the initial inhomogeneities or BHs formed in trans-Planckian particle collisions. Both of these are hypothetical classes, but may explain some of the observed phenomena.

BH solutions have a typical peculiar structure, containing a singularity at their core and possessing an event horizon at a certain radius from their core. This curvature singularity is a region where the spacetime curvature becomes infinite; thus, the singularity remains even if the coordinate system is changed. For non-rotating BHs this singularity takes the shape of a single point; for rotating BHs, however, due to the spinning, the singularity has the shape of a ring. The event horizon is a boundary in spacetime where matter and light can get through it - only in one direction - going towards the "centre" of the BH; it can never exit from it thereafter. This name is derived from the fact that if an event occurs within this boundary, an outside observer cannot get information about that event: it is beyond the "horizon". As we will see in the following sections, the event horizon is also a singularity in the simplest known coordinate system that describes BH solutions. However, what distinguish it from the central singularity, is the fact that is possible to make it regular by changing the coordinate system, in other words, it is a coordinate singularity.

According to the standard General Relativity paradigm, to describe a BH system we have to pay attention to three important independent physical properties: the mass M, the charge Q and the angular momentum J. This is the statement of the uniqueness theorems [14]. Depending on the value of these parameters we can have four types of stationary BHs: the Schwarzschild BH $(M, J = 0, Q = 0)$, the Reissner-Nordström BH $(M, J = 0, Q \neq 0)$, the Kerr BH $(M, J \neq 0, Q = 0)$ and Kerr-Newman BH $(M, J \neq 0, Q \neq 0)$. For this set of parameters a BH solution exists if the inequality $M \geqslant \sqrt{a^2 + Q^2}$ is obeyed, where we set $G = c = 1 = 4\pi\epsilon_0$ and $a = J/M$. Otherwise the solution describes a "naked" singularity, *i.e.*, a spacetime geometry where the curvature singularity is not cloaked by an event horizon.

Up to this point, we have discussed BHs using classical (relativistic) physics only. However, relevant research about quantum effects in BH physics started to appear in the 1970s [15]. The most well-known effect is probably the Hawking radiation predicted by Stephen Hawking in 1974 [16]. Due to the creation of pairs of particles from quantum vacuum fluctuations, one portion of these particles escapes towards infinity while the other portion is trapped inside the BH horizon. The particles that escape from the BH form a radiation, the so called Hawking radiation. This radiation reduces the mass of the BH steadly over time, in a process that became known as "BH evaporation". This effect is particularly important for small-mass primordial BHs, because they possess a high Hawking temperature (the Hawking temperature is inversely proportional to the BH mass), which means an increase in Hawking radiation.

In 1973, Bardeen, Carter and Hawking [17] formulated a set of laws of BH mechanics that presented a close resemblance to the laws of ordinary thermodynamics. This work built on intriguing observations by Bekenstein, suggesting that the BH horizon area should play the role of an entropy for BHs [18]. The prediction of Hawking radiation, in the following year, showed that this was no mere analogy; indeed BHs are thermodynamical systems and the entropy of the BH is proportional to its horizon area. This far reaching discovery, however, led to some problems that still linger today. One of these problems is the microscopic origin of the entropy. Another problem, is the so-called *information-loss*

paradox [19]: if the BH radiation is thermal and the BH evaporates completely, this evolution can transform pure states into mixed states, which entangles a non-unitary evolution from the viewpoint of quantum mechanics and information loss.

These problems have triggered much work. One research direction has been to consider models of compact objects without an event horizon. In the next chapter we will discuss some models of such "exotic" compact objects (ECOs) and their properties.

2.2 The Kerr-Newman solution

The most general (single) BH solution, within General Relativity and assuming electro-vacuum, is given by the Kerr-Newman metric which describes a charged spinning BH. This solution was found by Newman *et al.* in [20], when they solved the coupled Einstein-Maxwell equations. The Kerr-Newman metric, with signature $(-,+,+,+)$, in Boyer-Lindquist coordinates, is given by [21]

$$ds^2 = -\frac{\Delta}{\Sigma}\left[dt - a\sin^2\theta\, d\phi\right]^2 + \frac{\Sigma}{\Delta}dr^2 + \Sigma\, d\theta^2 + \frac{\sin^2\theta}{\Sigma}\left[a dt - \left(r^2+a^2\right)d\phi\right]^2, \tag{2.2}$$

where $\Delta \equiv r^2 - 2Mr + a^2 + Q^2$ and $\Sigma \equiv r^2 + a^2\cos^2\theta$. From this metric one can obtain the other stationary solutions in (electro-)vacuum as special cases, as we now discuss.

2.2.1 Special cases

Schwarzschild BH

The Schwarzschild BH solution can be obtained when in (2.2) $a = 0$ and $Q = 0$; it is the most simple solution of a stationary (in this case, actually, static) BH. This solution describes the vacuum region exterior to a spherical object (Birkhoff's theorem). The event horizon is located at the so-called Schwarzrschild radius, $r_S = 2M$. The metric possess two singularities at $r =$constant surfaces, one at r_S and the other at the center of the BH, $r = 0$. If an appropriate change of coordinates is applied to this solution, the singularity at r_S can be removed, and this surface becomes regular. Thus, $r = r_S$ was merely a coordinate singularity. However, one cannot say the same about the singularity at $r = 0$. This can be seen by calculating a curvature invariant. The Kretschmann invariant is an example of a curvature invariant, and for the Schwarzschild metric it is given by [13]

$$R_{\mu\nu\lambda\rho}R^{\mu\nu\lambda\rho} = \frac{12r_S^2}{r^6}, \tag{2.3}$$

where $R_{\mu\nu\lambda\rho}$ is the Riemann curvature tensor. We can see that if $r = r_S$ then the curvature invariant is finite, but if $r = 0$ then we have an infinite curvature, showing this point is a true, physical singularity. This type of physical singularity cannot be removed by any coordinate transformation.

This solution has some interesting properties, specially near the horizon. Considering an object at rest, in Schwarzschild coordinates, its proper time $d\tau$ on a Schwarzschild metric is given as [22]

$$d\tau = \left(1 - \frac{2M}{r}\right)^{\frac{1}{2}} dt. \tag{2.4}$$

One observes from (2.4), that the proper time coincides with the coordinate time t at spatial infinity. When an object approaches the horizon, r_S, dt tends to infinity. For a distant observer, this implies, analysing the geodesic equations, that an infalling object never seems to reach the event horizon r_S, giving the impression that it moves increasingly slowly as it approaches it.

Another perspective on this effect is the near horizon redshift, that has unusual peculiarities. The redshift, z, is given by [22]

$$1 + z = \left(1 - \frac{2M}{r}\right)^{-\frac{1}{2}}. \tag{2.5}$$

When $r \to r_S$, z tends to infinity. Near the horizon, objects are infinitely redshifted.

An interesting feature of the Schwarzschild BH is the possibility of having stable circular orbits. For a massive particle, these orbits are located at $r \geq 3r_S$ where at $r = 3r_S$ is the innermost stable circular orbit (ISCO). In the case of light, there is a circular orbit located at $r = 1.5r_S$; however, it is unstable.

Reissner-Nordström BH

Like the Schwarzschild solution, the Reissner-Nordström metric [23, 24] is a spherically symmetric solution and it is given by (2.2) when $a = 0$. This solution is not a vacuum solution due to the presence of an electromagnetic field that is originated by the non-null electric charge Q.

The Reissner-Nordström solution, in the coordinates (2.2) has three singularities at constant r: at $r = 0$, $r_- = M - \sqrt{M^2 - Q^2}$ and $r_+ = M + \sqrt{M^2 - Q^2}$ where the first one is a curvature singularity and the other two are coordinate singularities. If in this solution $M^2 > Q^2$, the two coordinate singularities have a special meaning - they are null surfaces corresponding to horizons. The larger one, r_+, is the outermost horizon or the event horizon, while the smaller one, r_-, is the innermost horizon also known as Cauchy horizon.

If $M^2 = Q^2$ we are facing an extremal Reissner-Nordström BH with only one (but degenerate) horizon at $r = M$. If $M^2 < Q^2$, the horizons $r_\pm$ are imaginary, which means that there are no coordinate singularities at constant r (except $r = 0$). Thus, this case describes a naked singularity. This last case is unlikely to emerge from gravitational collapse. Indeed, according to a well known conjecture (albeit with substantial evidence), *the cosmic censorship hypothesis* [25], naked singularities – *i.e.* that are not cloacked by a horizon – cannot form from gravitational collapse in an asymptotically flat spacetime that is non-singular on some initial spacelike hypersurface (Cauchy surface).

Kerr BH

The Kerr BH solution, was found by Roy Kerr in 1963 [26], and describes the vacuum solution of an uncharged rotating BH. This stationary axisymmetric vacuum solution can be obtained by setting $Q = 0$ in (2.2). Similarly to the Reissner-Nordström solution, it possesses three singularities: one is located at the "center" $r = 0$ (and $\theta = \pi/2$) - a curvature singularity - and the other two at $r_- = M - \sqrt{M^2 - a^2}$ (inner horizon) and at $r_+ = M + \sqrt{M^2 - a^2}$ (outer/event horizon) -, which are coordinate singularities. The case $M = a$, describes an extremal Kerr BH. For $M < a$, the horizons are imaginary, the Kerr solution is *overspinning* and it describes a naked singularity.

One interesting feature in this solution is the occurrence of a phenomenon called *frame-dragging*. Consider a particle that falls radially towards the BH, starting from spatial infinity, without angular momentum. The infalling particle gains angular motion, whose angular velocity, seen by an observer at spatial infinity is given by

$$\Omega(r, \theta) = \frac{d\phi}{dt} = \frac{2Mar}{(r^2 + a^2) - a^2 \Delta \sin^2 \theta} \ . \tag{2.6}$$

Thus, as it approaches the BH, the particle will tend to be dragged along the same direction in which the BH rotates. For it to keep stationary relatively to the distant stars a force to contradict this tendency is required. Mathematically, this phenomenon is associated to the existence of off-diagonal terms in the Kerr metric.

The Kerr BH has a special region, wherein is impossible to counteract its rotation. When an object comes from infinity, at a certain distance from the BH, there is a surface called *ergosurface*, beyond which the object cannot avoid moving in the angular direction, as seen from the observer at infinity. This surface is not a horizon because particles can get out from this surface; however there is nothing that can be done to prevent angular motion. The space between the event horizon and the ergosurface is called *ergoregion*, whose in Boyer-Lindquist radial coordinate is given as

$$r_e(\theta) = M + \sqrt{M^2 - a^2 \cos^2 \theta} \ . \tag{2.7}$$

At $\theta = 0$ and $\theta = \pi$ the ergosurface coincides with the event horizon but at other values of θ it lies outside of the event horizon. Theoretically, the extraction of energy and mass from a rotating BH is

possible due to the presence of this region. In the ergoregion there may be particles with local positive energy but which are seen as having negative energy by the observer at spatial infinity, due to the fact that the timelike Killing vector (at infinity), which is associated to the coordinate t, is spacelike in the ergoregion.

Considering a particle, with a certain positive energy (from the viewpoint of the observer at infinity), that is thrown into the ergoregion. Inside the ergoregion, this particle decays into two other particles, one of which escapes from the ergosphere with a greater energy than the original one, while the other has a negative energy (from the viewpoint of the observer at infinity) and falls into the BH. Thus, the observer at infinity will see this process as extracting the BH's energy. This process is called *Penrose process* and it was suggested by Roger Penrose in 1969 [27].

2.2.2 Properties of the Kerr-Newman solution

The Kerr-Newman solution has similar properties to those of the Kerr solution [20, 21]. This solution possesses three r =constant singularities: two coordinates singularities, one at $r_- = M - \sqrt{M^2 - a^2 - Q^2}$ and the other at $r_+ = M + \sqrt{M^2 - a^2 - Q^2}$, where the event and Cauchy horizon are located respectively; and one curvature singularity at $r = 0$ and $\theta = \pi/2$. As for Kerr, the curvature singularity does not have a point-like shape, but rather a ring-like shape. This can be seen explicitly by changing to Kerr-Schild coordinates, where the singularity will be on a circle of radius a around the origin in the z-plane.

The extremal Kerr-Newman BH occurs when $M = \sqrt{a^2 + Q^2}$ with one degenerate event horizon at $r = M$. For $M < \sqrt{a^2 + Q^2}$, the roots of $\Delta = 0$ are not real, making the curvature singularity naked. As we have seen before, this naked singularity leads to the violation of the cosmic censorship conjecture.

The Kerr-Newman solution also contains an ergoregion. The ergosurface's location, r_e, can be calculated through the vanishing of the time-time metric component,

$$0 = g_{tt} = \Sigma \left(r^2 + a^2 \cos^2 \theta - 2Mr + Q^2 \right) . \tag{2.8}$$

At infinity for $g_{tt} < 0$, the world-line of a particle at constant (r, θ, ϕ) is timelike; however for $g_{tt} > 0$ the world-line is spacelike. So at $g_{tt} = 0$ we obtain the ergosurface's equation, which for the Kerr-Newman BH takes the form

$$r_e \left(\theta \right) = M + \sqrt{M^2 - a^2 \cos^2 \theta - Q^2}. \tag{2.9}$$

There is also another solution to the quadratic equation $g_{tt} = 0$. However it lies inside the horizon.

2.2.3 Uniqueness theorems

The importance of the Kerr(-Newman) solution is intrinsically connected to the fact that rather than describing one BH solution it describes *the only* (single) BH solution of Einstein's equations in (electro-)vacuum. This is established by the *uniqueness theorems*. But before describing these theorems, let us write some definitions, from [25], that are essential to understand the theorems.

Definition: An asymptotically flat spacetime is stationary if and only if there exists a Killing vector field, k, that is timelike near ∞ (where we may normalize it such that $k^2 \to -1$), i.e. outside a possible horizon, $k = \partial/\partial t$ where t is a time coordinate. The general stationary metric in these coordinates is therefore

$$ds^2 = g_{tt} \left(\vec{x} \right) dt^2 + 2 g_{t\mu} \left(\vec{x} \right) dt dx^\mu + g_{\mu\nu} \left(\vec{x} \right) dx^\mu dx^\nu . \tag{2.10}$$

A stationary spacetime is static at least near ∞ if it is also invariant under time-reversal. This requires $g_{t\mu} = 0$, so the general static metric can be written as

$$ds^2 = g_{tt} \left(\vec{x} \right) dt^2 + g_{\mu\nu} \left(\vec{x} \right) dx^\mu dx^\nu , \tag{2.11}$$

for a static spacetime outside a possible horizon.

Definition: An asymptotically flat spacetime is axisymmetric if there exists a Killing vector field m (an 'axial' Killing vector field) that is spacelike near ∞ and for which all orbits are closed.

We can choose coordinates such that

$$m = \frac{\partial}{\partial \phi}, \tag{2.12}$$

where ϕ is a coordinate identified modulo 2π, such that $m^2/r^2 \to 1$ as $r \to \infty$. Thus, as for k, there is a natural choice of normalization for an axial Killing vector field in an asymptotically flat spacetime.

Thus the Schwarzschild metric, say, is static, whereas the Kerr metric is stationary but not static.

In 1923 Birkhoff [28] proved a theorem, designated as *Birkhoff's theorem*, showing that spherically symmetric solutions of Einstein's field equations in vacuum are static and asymptotically flat. This means that the metric outside a star is described by the Schwarzschild metric. A generalization of this theorem exists for the Einstein-Maxwell field equations, which shows that the only spherically symmetric solution is the Reissner-Nordström BH [25].

Birkhoff's theorem shows that, in General Relativity, spherical symmetry (in vacuum) implies staticity. How about the converse? Does staticity imply spherical symmetry? Surprisingly, for BHs it does! This is the content of *Israel's theorem* [29]: if a metric describes an asymptotically flat, static, vacuum spacetime that is non-singular on and outside an event horizon, then the metric is Schwarzschild. This was the first version of the *a uniqueness theorem*.

However these two theorems are not applicable to axisymmetric solutions of Einstein field equations. A theorem similar to Israel's theorem was proposed by Carter [30] and Robinson [31]. They proved that if a metric describes an asymptotically flat stationary and axisymmetric vacuum spacetime that is non-singular on and outside an event horizon, then the metric is a member of the two-parameter $(M,\ J)$ Kerr family. This theorem is designated as *Carter-Robison theorem* and can be generalized to Kerr-Newman solution with three parameters $(M,\ J,\ Q)$ [25].

2.3 A scalar field on the Kerr-Newman background

The study of fields in BH spacetimes has been a popular area of research for a few decades. This led to the discovery of some new features in the BH physics. In this section we will derive the equations of a massive and charged *test* scalar field in a Kerr-Newman spacetime.

Let us consider a physical system that consists of a massive, charged scalar field minimally coupled to the Kerr-Newman BH, where its spacetime is described by the line element in (2.2). The dynamics of this system is described by the Klein-Gordon equation

$$\left(\nabla^\nu - iqA^\nu\right)\left(\nabla_\nu - iqA_\nu\right)\Psi - \mu^2\Psi = 0, \tag{2.13}$$

where q is the scalar field charge, μ the scalar field mass and A_ν is the electromagnetic 4-potential given by

$$A_\nu = \left(-\frac{rQ}{\Sigma}, 0, 0, \frac{aQr\sin^2\theta}{\Sigma}\right). \tag{2.14}$$

To solve this equation we can decompose the scalar field as Fourier modes in the form

$$\Psi\left(t, r, \theta, \phi\right) = \sum_{l,m} e^{-i\omega t + im\phi} F_{lm}\left(r, \theta\right). \tag{2.15}$$

where $\omega > 0$ (to focus on future directed modes), $l \in \mathbb{N}_0$ and $m \in \mathbb{Z}$. Here ω is the mode's frequency. The separation of t and ϕ is due to the existence of two Killing vectors, $\partial/\partial t$ and $\partial/\partial\phi$, for the Kerr-Newman metric.

Using the metric components of the line element (2.2) in (2.13) and using the ansatz (2.15) (omiting the arguments of F), we obtain the equation,

$$\left[\frac{\left(r^2+a^2\right)^2}{\Delta}-a^2\sin^2\theta\right]\omega^2+\left[\frac{a^2}{\Delta}-\frac{1}{\sin^2\theta}\right]m^2+2\left[-\frac{a\left(r^2+a^2\right)}{\Delta}+a\right]m\omega+\frac{1}{F}\frac{\partial}{\partial r}\left(\Delta\frac{\partial F}{\partial r}\right)$$
$$+\frac{1}{F\sin\theta}\frac{\partial}{\partial\theta}\left(\sin\theta\frac{\partial F}{\partial\theta}\right)+\frac{q^2Q^2r^2}{\Delta}+\frac{2qQr}{\Delta}\left[-\omega\left(r^2+a^2\right)+am\right]=\mu^2\left(r^2+a^2\cos^2\theta\right). \tag{2.16}$$

We observe, from this equation, that the dependence in r and θ can be separated, so we can take $F_{lm}(r,\theta)=R_{lm}(r)\,S_{lm}(\theta)$. By performing this separation the partial derivatives become total derivatives in (2.16).

Separating the dependences in r and θ to different sides of the equation and changing $\omega^2a^2\sin^2\theta=\omega^2a^2\left(1-\cos^2\theta\right)$ we obtain two coupled ordinary differential equations. To separate them we can introduce a constant, denoted as $-\lambda_{lm}$, where each side of the equation must be equal. The first equation is only dependent of the angular variable and is given by

$$\frac{1}{\sin\theta}\frac{d}{d\theta}\left(\sin\theta\frac{dS(\theta)}{d\theta}\right)+\left\{a^2\cos^2\theta\left(\omega^2-\mu^2\right)-\frac{m^2}{\sin^2\theta}+\lambda_{lm}\right\}S(\theta)=0. \tag{2.17}$$

The functions $S_{lm}(\theta)$ that solve this equation are called (scalar) *spheroidal harmonics* [32]. This equation can be solved by expanding the separation constant as a power series of the form

$$\lambda_{lm}=l(l+1)+\sum_{k=1}^{\infty}c_k\;a^{2k}\left(\omega^2-\mu^2\right)^k. \tag{2.18}$$

Here, $a^2\left(\omega^2-\mu^2\right)$ is the degree of spheroidicity and c_k are (l,m)-dependent coefficients that can be found in [32]. Note that for $a=0$ this equation reduces to the familiar associated Legendre equation and the solutions are the well-known spherical harmonics (the θ-dependent part).

The second equation only depends on the radial coordinate, r, and takes the form of

$$\frac{d}{dr}\left(\Delta\frac{dR(r)}{dr}\right)+\left\{\frac{\left[\omega\left(r^2+a^2\right)-am-qQr\right]^2}{\Delta}-\omega^2a^2+2am\omega-\mu^2r^2-\lambda_{lm}\right\}R(r)=0, \tag{2.19}$$

where λ_{lm} is given by (2.18).

In our study we are only interested in solving the radial equation (2.19). But first we need to impose some physical boundary conditions. Due to the presence of a BH, we only have purely ingoing waves at the horizon. The shape of this wave can be calculated by introducing the 'tortoise' coordinate, r_*, into (2.19), where

$$\frac{dr_*}{dr}=\frac{r^2+a^2}{\Delta}. \tag{2.20}$$

We observe that this change of coordinate only covers the outside of the BH ($r\in[r_+,+\infty]\;\Rightarrow\;r_*\in[-\infty,+\infty]$). Taking $r\to r_+$ the radial solution behaves as

$$R_{lm}(r)\approx e^{-i\left(\omega^2-\omega_c^2\right)r_*}, \tag{2.21}$$

where w_c is the critical frequency and is defined as

$$\omega_c=\frac{am}{r_+^2+a^2}+\frac{qQr_+}{r_+^2+a^2}. \tag{2.22}$$

Another physical boundary condition we need to impose is at spatial infinity. The field, asymptotically, decays like

$$R_{lm}\approx A\frac{e^{-\sqrt{\mu^2-\omega^2}r}}{r}+B\frac{e^{\sqrt{\mu^2-\omega^2}r}}{r}. \tag{2.23}$$

Depending on the sign of $\mu^2 - \omega^2$ these exponentials may describe ingoing/outgoing waves or decay/growing solutions. Here A, B are constants. For $\mu^2 > \omega^2$ we have asymptotically decaying (quasi-)bound states (taking $B = 0$). For $\mu^2 < \omega^2$ we have asympotic waves, which is appropriate to describe scattering problems (wherein both A and B are non-vanishing) and also Quasi-Normal Modes (QNMs) problems (wherein only an outgoing wave at infinity exists). In the latter case, as well as in the quasi-bound state case the frequencies are complex, having a real part, ω_R, and an imaginary part, ω_I.

2.3.1 Superradiance

Superradiance is a phenomenon where the radiation is amplified when interacting with a rotating object. This can also occur on a BH due to the dissipation at the event horizon that permits the field to extract energy, charge and angular momentum from the BH. For a Kerr-Newman BH, superradiance occurs when the following condition is satisfied

$$0 < \omega < m\Omega_H + q\Phi_H \equiv \omega_c, \tag{2.24}$$

where Ω_H is the angular velocity of the event horizon and Φ_H is the electrostatic potential of the horizon. From inspection of equation (2.22), these parameters take the form

$$\Omega_H = \frac{a}{r_+^2 + a^2} \quad \text{and} \quad \Phi_H = \frac{Qr_+}{r_+^2 + a^2}. \tag{2.25}$$

The amplification of the scattered wave can be computed through a factor denoted as Z_{slm} where s is the spin of the field. For a scalar field, $s = 0$, the amplification factor is given by the formula

$$Z_{0lm} = \frac{|A_{out}|^2}{|A_{in}|^2} - 1, \tag{2.26}$$

where A_{in} is the ingoing wave amplitude whereas A_{out} is the outgoing wave amplitude. In [33] this amplification factor was obtained for a massless scalar field in a Kerr spacetime, analytically, in the regime of low frequencies $M\omega \ll 1$, resorting to the matching procedure to calculate the wave amplitudes. The amplification factor, Z_{0lm}, was then given by

$$Z_{0lm} = -4L \left[\frac{(l!)^2}{(2l)!\,(2l+1)!!} \right]^2 \prod_{n=1}^{l} \left(1 - \frac{4L^2}{n^2} \right) \left[\omega \left(r_+ - r_- \right) \right]^{2l+1}, \tag{2.27}$$

where $L = \left(r_+^2 + a^2 \right) (\omega - m\Omega_H) / (r_+ - r_-)$. Here we observe that $Z_{0lm} > 0$ due to $\omega < m\Omega_H$. Note that for $Z_{0lm} > 0$ implies that $|A_{out}|^2 > |A_{in}|^2$ (see (2.26)), which means the wave is superradiantly amplified.

Under certain circumstances, the superradiant amplification can lead to an instability of a BH. For this to occur, the scalar field must be confined in the vicinity of the BH, such that the superradiant amplification occurs repeatedly leading to an exponentially growing energy extraction from the BH. The mass of a scalar field introduces a potential barrier at infinity, and can thus act like a mirror for low frequency modes, thus leading to a superradiant instability in the Kerr-Newman geometry. Remarkably, at the threshold of unstable modes, there are genuine bound states in a BH background as we will review in the next section.

2.3.2 Stationary Scalar clouds

When the scalar field frequency is equal to critical frequency (resonance condition),

$$\omega = \omega_c, \tag{2.28}$$

there are bound states, resembling atomic orbitals, which are called *stationary scalar clouds*. These stationary clouds are characterized by a set of integer "quantum" numbers (n, l, m) and have real

frequency. At spatial infinity they decay asymptotically. We emphasise these bound states exist at the maximal threshold of the superradiant unstable modes.

The massive scalar field equation, at these resonances, has simple solutions if we specialise to the case of the extremal Kerr BH. This case was studied in [34], where the stationary scalar clouds were obtained in closed form in the whole spacetime. Considering the Kerr BH, given by (2.2) with $Q=0$, the radial equation takes the form

$$\frac{d}{dr}\left(\Delta\frac{dR\left(r\right)}{dr}\right)+\left\{\frac{\left[\omega\left(r^{2}+a^{2}\right)-am\right]^{2}}{\Delta}-\omega^{2}a^{2}+2am\omega-\mu^{2}r^{2}-\lambda_{lm}\right\}R\left(r\right)=0. \tag{2.29}$$

In the extremal case, $a=M$ and the resonance condition will be simplified to $\omega=m\Omega_{H}=m/2M$. Putting this conditions in (2.29); changing the dependent variable $R\left(r\right)$ to $W\left(r\right)$ through $R\left(r\right)=MW\left(r\right)/\left(r-M\right)$; and redefining the independent variable to $xM=r-M$ (where $0\leq x<\infty$) we can obtain a Hydrogen-like Schrödinger radial equation given as

$$\left[-\frac{d^{2}}{dx^{2}}+\frac{\left(2M^{2}\mu^{2}-m^{2}\right)}{x}+\frac{\left(\lambda_{lm}+\mu^{2}M^{2}-\frac{7}{4}m^{2}\right)}{x^{2}}\right]W\left(x\right)=\left(\frac{m^{2}}{4}-\mu^{2}M^{2}\right)W\left(x\right). \tag{2.30}$$

We observe that there are two different cases corresponding to the signs of $m^{2}/4-\mu^{2}M^{2}$. In terms of frequency this is $\left(\omega^{2}-\mu^{2}\right)M^{2}$, and if $\omega^{2}<\mu^{2}$ (negative sign) we have the bound states and if $\omega^{2}>\mu^{2}$ (positive sign) we have the scattering states. Since we are interested in the bound states we will consider the first case. Redefining $m^{2}/4-\mu^{2}M^{2}$ as $\epsilon\equiv\sqrt{\mu^{2}M^{2}-m^{2}/4}$ the equation (2.30) has the form of the Whittaker's equation [32],

$$z^{2}\frac{d^{2}W\left(z\right)}{dz^{2}}=\left[\frac{z^{2}}{4}-kz+\left(p^{2}-\frac{1}{4}\right)\right]W\left(z\right), \tag{2.31}$$

with

$$z\equiv2\epsilon x,\quad k\equiv\frac{m^{2}}{4\epsilon}-\epsilon,\quad p^{2}\equiv\lambda_{lm}+\epsilon^{2}-\frac{3}{2}m^{2}+\frac{1}{4}. \tag{2.32}$$

Whittaker's equation has solution of confluent hypergeometric type with a regular singular point at $z=0$ and an irregular singular point at $z=\infty$. The bounded solutions of Whittaker's equation, as $z\to\infty$, have the form

$$W\left(z\right)=z^{p+1/2}e^{-z/2}\sum_{j}a_{j}z^{j}, \tag{2.33}$$

where the series must be finite. To archive the finiteness of the series a quantization condition

$$k=\frac{1}{2}+p+n,\quad n\in\mathbb{N}_{0}, \tag{2.34}$$

must be obeyed. Here $p\geq1/2$ due to the regularity at the event horizon, which implies that $k>0$. Taking account of this condition, the bound states resonances must lie in the band

$$\frac{m}{2}<\mu M<\frac{m}{\sqrt{2}}. \tag{2.35}$$

With these conditions in mind it is possible to extend the quantization condition in terms of ϵ where it is possible to obtain the polynomial equation

$$\begin{aligned}m^{4}-4m^{2}\left(2n+1\right)\epsilon+16\left[m^{2}+\left(n+\frac{1}{2}\right)^{2}-\left(l+\frac{1}{2}\right)^{2}\right]\epsilon^{2}\\+16\left(2n+1\right)\epsilon^{3}-16\epsilon^{2}\sum_{k=1}^{\infty}c_{k}\left[-\epsilon^{2}\right]^{k}=0,\end{aligned} \tag{2.36}$$

which describes the family of stationary regular field configurations in the extremal Kerr BH. This polynomial equation can be solved numerically by a root finding procedure. The Kerr-Newman scalar clouds were studied in [35] numerically.

Chapter 3

Exotic compact objects

3.1 Overview

What if astronomical BH candidates in fact did not have an event horizon? This sounds like a leap of faith, because event horizons are predicted by the simplest and most natural solutions of classical General Relativity that describe compact objects, such as the Kerr-Newman BH family we have discussed in the last chapter. However, these solutions have issues. Classically, they contain singularities, hinting at a breakdown of the classical theory. Quantum mechanically, they lead to problems, such as the BH information loss paradox. None of these issues is, by any means, ruling out the standard General Relativity BHs as an accurate description of the astrophysical BH candidates. But these issues suggest one should explore alternative models for compact objects, even if just to establish that there are no viable alternatives. This line of research has been pursued over the years in a number of works – see *e.g.* [1–3, 36–48].

Horizonless exotic compact objects (*ECOs*), are theoretically suggested objects, similar to BHs in the sense of being very compact and thus exerting strong gravity effects, but they have neither an event horizon nor a curvature singularity. Examples of ECOs include:

i) *boson stars*; these are a type of everywhere regular gravitating solitons, first derived for scalar fields long ago [41, 42], and more recently derived also for massive vector fields [43]. They can be regarded as a type of macroscopic Bose-Einstein condensates [44]. Some boson stars are known to be perturbatively stable and they have even been evolved in binaries using Numerical Relativity techniques [45]. There are both spherically symmetric (static) solutions, as well as axisymmetric (rotating) solutions;

ii) *gravastars*; these ECOs were proposed in [39]. The model describes an object composed by a segment of de Sitter space in its interior while the exterior is described by the Schwarzschild spacetime. The would-be horizon is a phase boundary consisting of a thin shell of matter;

iii) *fuzzballs*; these were proposed in [40]. The fuzzball is composed of a ball of strings instead of an event horizon and does not possess a singularity at its center;

iv) *wormholes*; these are topologically non-trivial configurations in which the horizon can be avoided. They are typically unstable [49].

The difference between ECO's and BHs is the absence/presence of event horizons. But in view of the observational illusiveness of the BH horizon, could we distinguish these different types of objects through observations, if they occur in Nature? With the detection of gravitational waves, BHs are entering an era of precision observations. However, no experiments have been able to probe the spacetime sufficiently near the event horizon, as to distinguish BHs from BH mimickers (*i.e* ECOs). In particular, it has been proposed [2, 36, 38] that it is possible to distinguish BHs from ECOs through the analysis of the gravitational wave signal: the final stage of the evolution is dominated by the QNMs and the spectrum of QNMs is different for each type of object (BHs or ECOs).

Although there are different proposed models for ECOs, in our study we will focus on a simple toy model that has been recently considered in the literature (see *e.g.* [2]). The main idea is that the ECO is characterised by the Kerr metric up to the vicinity of the (would-be) horizon. Instead of having a horizon, however, the ECO has a surface wherein reflective boundary conditions are imposed (see Fig. 3.1). In this work, we shall not be interested in what is the fundamental origin of this model, or how it is completed inside the reflective surface, but rather on what are its consequences, in particular when interacting with a test scalar field.

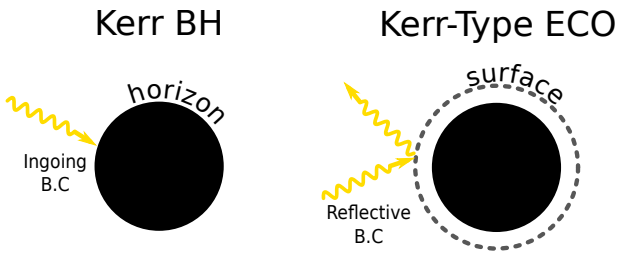

Figure 3.1: An illustrative scheme of a Kerr BH and a Kerr-type ECO (Top view). Here we represent the difference in behavior at the surface on both compact objects. For the BH the existence of a horizon implies ingoing boundary conditions whereas for the ECO the presence of a reflective surface implies reflective boundary conditions.

As we discussed in the previous chapter, the Kerr(-Newman) solution is prone to superradiant instabilities. These can also occur for rotating ECOs of the sort we have just described, when they spin very fast and are sufficiently compact. In [2] it was demonstrated numerically that these objects may become unstable to scalar perturbation modes, due to the superradiant phenomenon. The same study also revealed that if the reflective surface is at a considerable distance from the would-be horizon, the ergoregion instability is quenched. These observation led Hod [1] to study, analytically, a unique family of critical (marginally-stable) ECOs that occur at the boundary between stable and unstable horizonless spinning configurations.

Following Hod's work, we will study, in the next two chapters, this unique family of critical (marginally-stable) ECOs on the Kerr-Newman spacetime for both electrically uncharged and charged scalar fields. But before we describe such study, we will present a no-hair theorem for spherically symmetric ECOs, also demonstrated by Hod in [4].

3.2 No-hair theorem for spherically symmetric ECOs

Consider a spherically symmetric ECO or star. Can it support a non-trivial profile of a real, massless scalar field under a totally reflective boundary condition on its surface? In [4], it was demonstrated that reflecting stars share the characteristic no-scalar-hair property of asymptotically flat spherical BHs (see [50] for a review). In a sense, this is surprising, since the no-hair property is typically attributed to the horizon boundary condition characteristic of BHs, *i.e* a purely ingoing wave at the horizon.

To establish this result, we shall consider a static spherically symmetric compact reflecting object with radius R. Assuming vacuum outside this radius, by Birkhoff's theorem, the outside line element is given by the Schwarzschild solution. In particular, its line element in Schwarzschild coordinates may be represented as,

$$ds^2 = -e^{\nu(r)}dt^2 + e^{\lambda(r)}dr^2 + r^2\left(d\theta^2 + \sin^2\theta d\phi^2\right). \tag{3.1}$$

Here $\nu \sim r^{-1}$ and $\lambda \sim r^{-1}$, when $r \to \infty$, obeying the asymptotically flatness condition. For brevity, we shall omit the arguments in ν and λ.

Real Scalar Field

Now let us couple the object to a real scalar field Ψ whose action is described by:

$$\begin{aligned} S &= S_{EH} + S_M \\ &= S_{EH} - \frac{1}{2}\int \left[\partial_\alpha \Psi \partial^\alpha \Psi + V\left(\Psi^2\right)\right]\sqrt{-g}d^4x, \end{aligned} \tag{3.2}$$

where S_{EH} is the Einstein-Hilbert action that yields the Einstein field equations through the variational principle, $g = det\left(g_{\mu\nu}\right)$ is the metric determinant and $V\left(\Psi^2\right)$ is the potential associated to the scalar field. This potential is assumed to be positive semidefinite and a monotonically increasing function (includes the massive case), which means that it must obey the conditions:

$$V(0) = 0 \quad \text{and} \quad \dot{V} = \frac{d\left[V\left(\Psi^2\right)\right]}{d\left(\Psi^2\right)} \geqslant 0. \tag{3.3}$$

Before proceeding to the theorem demonstration, we still have to describe the scalar field in the exterior spacetime of the compact star. One can deduce the behavior at spatial infinity through the scalar field energy density, ρ. For an asymptotically flat spacetime with finite mass, the energy density should behave as $r^3\rho \to 0$ for $r \to \infty$. The energy density is related to the energy-momentum tensor, $T_{\mu\nu}$, through $\rho \equiv -T^t_t = -g^{tt}T_{tt}$, where

$$T_{\mu\nu} = -2\frac{1}{\sqrt{-g}}\frac{\delta S_M}{\delta g^{\mu\nu}}. \tag{3.4}$$

Then the energy density will be given as,

$$\rho = \frac{1}{2}\left[e^{-\lambda}\left(\Psi'\right)^2 + V\left(\Psi^2\right)\right]. \tag{3.5}$$

Taking in consideration the conditions (3.3) and the energy density behavior at spatial infinity, from (3.5) one can deduce that the scalar field at infinity behaves as $\Psi\left(r \to \infty\right) \to 0$. At the surface of the compact star, it is assumed that the scalar field should vanish, $\Psi\left(r = R\right) = 0$.

The action (3.2), yields the radial differential equation,

$$\partial_\alpha \partial^\alpha \Psi - \dot{V}\Psi = 0. \tag{3.6}$$

From this equation we can calculate the radial equation associated to the spacetime of the static spherically symmetric compact reflecting object, which takes the form of

$$\Psi'' + \frac{1}{2}\left(\frac{4}{r} + \nu' - \lambda'\right)\Psi' - e^\lambda \dot{V}\Psi = 0. \tag{3.7}$$

Analysing the boundary conditions imposed, the scalar field Ψ should have at least one extremum point, r_p at the interval $r_p \in [R, \infty[$, that should obey the following relations:

$$\left\{\Psi' = 0 \text{ and } \Psi \cdot \Psi'' < 0\right\} \quad \text{for} \quad r = r_p. \tag{3.8}$$

If, say, $\Psi'' < 0$ at $r = r_p$, these relations imply that,

$$\Psi'' + \frac{1}{2}\left(\frac{4}{r} + \nu' - \lambda'\right)\Psi' - e^\lambda \dot{V}\Psi < 0 \quad \text{for} \quad r = r_p, \tag{3.9}$$

which is in contradiction with the radial equation (3.7). On the other hand, if $\Psi'' > 0$ at $r = r_p$ one obtains the opposite inequality in (3.9), again in contradiction with the equation of motion. Thus, no such extremum point can exist; the only possible solution is $\Psi = 0$ everywhere, and the field is trivial.

In [4] it is concluded that these spherically symmetric compact reflecting objects cannot support static bound-state configurations made of the scalar fields whose potential $V\left(\Psi^2\right)$ is a monotonically

increasing function. Ruling out, in particular, the existence of asymptotically flat massive scalar "hair" outside the surface of a spherically symmetric compact reflecting star.

A few remarks about this result. Firstly, in hindsight the result is quite natural. The scalar field vanishes both at the star's surface as well as at spatial infinity. A non-trivial configuration thus requires the existence of an extremum in between. Like a string with two fixed ends that is raised above its equilibrium configuration by pulling it somewhere in the middle, the existence of such scalar field static configuration would require an exterior force to hold it in such non-equilibrium configuration.

Two possible ways to circumvent this theorem immediately come to mind: 1) consider a complex scalar field with a harmonic time dependence, like in the case of the stationary clouds discussed in the last chapter; 2) consider a charged scalar field in a charged star background. We shall now consider the former case, whereas the latter will be considered in Chapter 5.

Complex scalar field with harmonic time dependence

Now let us consider the same spherically symmetric compact reflecting object non-linearly coupled to a complex scalar field with a harmonic time dependence given as

$$\Psi = e^{-iwt} F(r), \tag{3.10}$$

whose action will be,

$$S = S_{EH} - \frac{1}{2}\int \left[\partial_\mu \Psi^* \partial^\mu \Psi + V\left(|\Psi|^2\right)\right] \sqrt{-g} d^4x, \tag{3.11}$$

where $V\left(|\Psi|^2\right)$ is the scalar field potential which is also positive semidefinite and monotonically increasing function, obeying the conditions (3.3).

The energy density for this scalar field is similar to (3.5) with an extra term due to the harmonic time dependence, where we have,

$$\rho = \frac{1}{2}\left\{ e^{-\lambda}\left[F'(r)\right]^2 + e^{-\nu}\omega^2\left[F(r)\right]^2 + V\left(\left[F(r)\right]^2\right) \right\}. \tag{3.12}$$

As we have seen, an asymptotically flat spacetime is characterized by an energy density that approaches zero asymptotically faster than $1/r^3$. In (3.12), this condition is possible if $F(r \to \infty) \to 0$. Also we make the same assumption that the scalar field should vanish at the surface of the compact object, $F(r = R) = 0$

From the action (3.11), we can obtain the equation,

$$\partial_\mu \partial^\mu \Psi - \dot{V}\Psi = 0. \tag{3.13}$$

Substituting the line element (3.1) in (3.13) for the complex scalar field Ψ we obtain the radial equation,

$$F''(r) + \frac{1}{2}\left(\nu' - \lambda' + \frac{4}{r}\right) F'(r) - e^{\lambda}\left(\dot{V} - e^{-\nu}\omega^2\right) F(r) = 0. \tag{3.14}$$

As we have seen before, the imposing boundaries at the scalar field, requires at least an extremum point, r_p, between the surface of the compact object and the spatial infinity. Then the radial part $F(r)$, at this extremum, is characterized by the same relations as (3.8). With these relations in mind and looking at the equation (3.14) we can conclude that this equation could be satisfied due to the extra term $e^{-\nu}\omega^2$.

Then we can say that the spherical symmetric reflecting compact star could support bound-states configurations made by the complex scalar field whose potential is a monotonically increasing function. Which means that, for a static spherically symmetric compact reflecting object coupled to a complex scalar field with a harmonic time dependence, the property of no-scalar-hair could not be established. We would like to emphasise that this result, to the best of our knowledge, has not been presented in the literature.

Although for the complex scalar field in study it was not possible to share the same no-scalar-hair property, some work has accomplish to generalized this theorem to other models, see [46–48]. In [46] it was demonstrated that for massive, real, scalar, vector and tensor fields the no-hair theorem can also be established for a static and stationary compact reflecting star. Also spacetimes with a cosmological constant were considered, generalizing this theorem. Following the work in [4], the same author proved the no-hair theorem for nonminimally coupled massless, real scalar fields, see [47], extending the above result to the massive case [48].

Chapter 4

Uncharged massless scalar field on a Kerr-Newman-type ECO

Does the no-scalar hair theorem that we have described in the previous chapter, Schwarzschild-type ECO for non-rotating ECOs, generalise to a rotating reflecting star? In this chapter we shall show that the answer is no. To do so, we shall follow [1] to obtain some explicit solutions of the scalar field on the background of an ECO that is described by the Kerr metric outside the reflecting surface. In order to understand the existence of these configurations, that are threshold modes of the superradiant instability, we shall also review the work [2] about the (in)stabilities of the horizonless Kerr-type ECOs with reflective surfaces linearly coupled to massless scalar fields.

A simple model was considered in [2] where the geometry outside the ECO is characterized by the Kerr geometry, and at a certain radius, r_0, there is a membrane with reflective properties which is above from the would-be horizon r_+. The membrane localization is given by the expression $r_0 = r_+ + \delta$, where the quantity $0 < \delta \ll M$. Although it does not contain a horizon, it has an ergoregion where the ergosphere is given by the expression (2.7). In order to study the (in)stabilities of these ECOs, the spacetime was subjected to scalar perturbations and reflective boundary conditions were imposed (Dirichlet or Neumann boundary conditions).

In [2] two cases were studied: ECOs with perfect reflective surface and ECOs with a slight absorption on the surface. For the perfectly reflecting surface, they found that at certain critical value of the spin the frequency is zero, which corresponds to the instabilities threshold. Above this critical value of the spin, the system suffers from ergoregion instability. This critical value depends on the ECO compactness, decreasing when $\delta \to 0$. Also they have shown that at the instabilities threshold, for a fixed value of the spin, there is a critical value of δ which above this value the ECO is stable.

When the reflective surface it is not perfect, this instability can be destroyed. They calculated that a small absorption at the level of $\sim 0.4\%$ the imaginary part of the frequency is always negative for any value of the spin, which means that ECOs can be stable against ergoregion instability.

Building upon this work, in [1] the author constructs a discrete spectrum of critical surface radii, for which the ECO can support spatially regular static scalar field configurations. The author also determines the maximal critical radius that determines the instabilities for a couple of spin values. In [3], the same author, constructs a discrete spectrum of critical surface radii for the regime of the super-extremal Kerr-type ECOs with reflective properties. There he found that the discrete spectrum is composed of a finite number of solutions of the resonance conditions, instead of the infinite discrete spectrum obtained in [1]

In the work below, we also present the existence of discrete set of critical surface radius in Kerr-Newman-type ECOs with reflective boundary conditions in the three different regimes: sub-extremal regime ($M > \sqrt{a^2+Q^2}$), extremal regime ($M = \sqrt{a^2+Q^2}$) and the super-extremal regime ($M < \sqrt{a^2+Q^2}$). These ECOs also support spatially regular static (marginally-stable) scalar field configurations. We remark that this provides a generalization of the results in [1] and [3] that consider $Q = 0$.

4.1 Setup

As in [1, 2], we shall assume an ECO with radius r_c and for $r > r_c$ the spacetime is characterized by the Kerr-Newman line element (2.2). The ECO radius is located at a microscopic distance above from the would-be horizon, r_+, and is characterized by the relation

$$z_c \equiv \frac{r_c - r_+}{r_+}. \tag{4.1}$$

Due to the location of the ECO surface radius relatively to the would-be horizon, we observe from (4.1) that the dimensionless parameter z_c is much smaller than 1 ($z \ll 1$). Also the ECO surface has reflective properties where its energy and angular momentum are neglected.

Submitting this system to a massless scalar field governed by the Klein-Gordon equation (2.13), we can decompose the scalar field like (2.15) and obtain a couple system of ordinary differential equations: (2.17) and (2.19). In this chapter, we set $\mu = 0$ and $q = 0$ in (2.13),(2.17) and (2.19). Also we will consider $M = 1$ for simplification.

With the radial equation determined we can now impose the boundary conditions. At the surface, due to the reflective properties, the ECO is characterized by (Dirichlet or Neumann) reflecting boundary conditions:

$$\begin{cases} R\left(r = r_c\right) = 0 & \text{Dirichlet B.C.;} \\ \frac{dR(r)}{dr}|_{r=r_c} = 0 & \text{Neumann B.C..} \end{cases} \tag{4.2}$$

Here the Dirichlet boundary condition implies that the wave is totally reflected with inverted phase, while the Neumann boundary condition implies that the wave is totally reflected in phase.

At spatial infinity the scalar modes are characterized by asymptotically decaying eigenfunctions of the form

$$R\left(r \to \infty\right) \to 0. \tag{4.3}$$

4.2 Sub-extremal Kerr-Newman

Let us start with the sub-extremal regime, $M > \sqrt{a^2 + Q^2}$. As discussed in [1] and [2], to obtain the discrete set of critical surface radius that marks the onset of superradiant instabilities in the curved spinning and charged spacetime, there is a unique family of static resonances that are characterized by the property

$$\omega = 0. \tag{4.4}$$

Imposing this property into (2.19), we obtain the simple ordinary differential equation

$$\frac{d}{dr}\left(\Delta \frac{dR\left(r\right)}{dr}\right) + \left\{\frac{a^2 m^2}{\Delta} - l\left(l+1\right)\right\} R\left(r\right) = 0. \tag{4.5}$$

Although it is perhaps not obvious in the form displayed, (4.5) has as solutions the hypergeometric functions, ${}_2F_1\left(a, b; c; z\right)$ [32]. To obtain a standard form of the hypergeometric differential equation from (4.5), we redefine the dependent variable $R\left(r\right)$ as well as the independent variable r with the following expression:

$$R\left(x\right) \equiv x^{-i\alpha}\left(1 - x\right)^{l+1} H\left(x\right), \tag{4.6}$$

where

$$x \equiv \frac{r - r_+}{r - r_-} \quad \text{and} \quad \alpha \equiv \frac{ma}{r_+ - r_-}. \tag{4.7}$$

Analysing the new independent variable x, we can observe that the would-be horizon is set at the origin whereas the exterior spacetime is now characterized by the interval $0 < x \leq 1$. Another observation is the fact that this change of variables is only valid for the non-extremal regime.

Applying these changes into (4.5), we obtain the characteristic hypergeometric differential equation

$$\begin{aligned} x\left(1-x\right)\frac{d^{2}H\left(x\right)}{dx^{2}}+\left[\left(1-2i\alpha\right)-\left(1+2\left(l+1\right)-2i\alpha\right)x\right]\frac{dH\left(x\right)}{dx} \\ -\left[\left(l+1\right)^{2}-2i\alpha\left(l+1\right)\right]H\left(x\right)=0, \end{aligned} \tag{4.8}$$

which solutions are a linear combination of hypergeometric functions. By substituting the solutions of (4.8) into (4.6), we obtain the radial equation

$$\begin{aligned} R\left(x\right)=&x^{-i\alpha}\left(1-x\right)^{l+1}\left\{A\ {}_{2}F_{1}\left(l+1-2i\alpha,l+1;2l+2;1-x\right)\right. \\ &\left.+B\left(1-x\right)^{-2l-1}\ {}_{2}F_{1}\left(-l-2i\alpha,-l;-2l;1-x\right)\right\}, \end{aligned} \tag{4.9}$$

where A and B are normalization constants.

Now let us impose the boundary condition (4.3). For $r\rightarrow\infty$ $(x\rightarrow1)$, the hypergeometric function behaves as ${}_{2}F_{1}\left(a,b;c;\left(1-x\right)\rightarrow0\right)\rightarrow1$ (see property Eq. 15.1.1 of [32]). The radial solution (4.9) will behave asymptotically as

$$R\left(x\right)\overset{x\rightarrow1}{=}A\left(1-x\right)^{l+1}+B\left(1-x\right)^{-l}. \tag{4.10}$$

At spatial infinity we observe from (4.10) that the first term is the only term that obeys condition (4.3) whereas the second term tends to infinity. So it is necessary that the second term vanishes at spatial infinity. Thus, B should vanish, $B=0$. Then the static resonances of the Kerr-Newman-type ECO is characterized by the radial function

$$R\left(x\right)=Ax^{-i\alpha}\left(1-x\right)^{l+1}\ {}_{2}F_{1}\left(l+1-2i\alpha,l+1;2l+2;1-x\right). \tag{4.11}$$

Note that the second term in (4.10) only tends to infinity if we consider $l>0$. For $l=0$ the second term is a constant and is given by the normalization constant B whereas the first term is zero. However, from (4.10) it is necessary that the radial function should vanish at spatial infinity, so even for $l=0$ requires $B=0$.

At last, when applying equation (4.11) into the reflective boundary conditions (4.2), we can obtain the following compact resonance equations:

$${}_{2}F_{1}\left(l+1-2i\alpha,l+1;2l+2;1-x_{c}\right)=0, \tag{4.12}$$

for a Dirichlet boundary condition and

$$\frac{d}{dx}\left[x^{-i\alpha}\left(1-x\right)^{l+1}\ {}_{2}F_{1}\left(l+1-2i\alpha,l+1;2l+2;1-x\right)\right]_{x=x_{c}}=0, \tag{4.13}$$

for a Neumann boundary condition.

4.2.1 Resonance spectra

The above process to obtain the compact resonance equations follows closely the one in [1], but with the generalisation that we have the Q^{2} term in $r_{\pm}$; thus, the solutions for the critical surface radius will be different when we change this parameter. These compact resonance equations can be easily solved numerically. For the given physical parameters $\{a,Q,l,m\}$ we obtain a discrete set of critical radii, which can support the spatially regular static (marginally-stable) scalar field resonances.

Through the outermost dimensionless critical surface radius, $z_{c}^{\max}$ we can study the (in)stabilities of the Kerr-Newman-type ECO. In [2] it was shown that for a fixing value of the angular momentum there is a critical radius which marks the boundary between stable and unstable Kerr-type ECOs. This means that for $r_{c}<r_{c}^{\max}$ the Kerr-type ECO suffers from superradiant instabilities whereas for

$r_c > r_c^{\max}$ the Kerr-type ECO is stable, as was concluded in [1]. Due to the fact that the dimensionless $z_c \ll 1$, in [2] was displayed the results in terms of z_c instead of r_c.

In Table 4.1 we display the outermost dimensionless radius $z_c^{\max}(a, Q, l, m)$ of the Kerr-Newman-type ECO that can support static massless scalar field configurations with reflective either Dirichlet or Neumann boundary conditions. This dimensionless radius depends on the angular momentum, a, the charge Q and the harmonic indices (l, m).

Dirichlet	$z_c^{\max}(a=0.3)$	$z_c^{\max}(a=0.5)$	$z_c^{\max}(a=0.7)$	$z_c^{\max}(a=0.9)$
$Q=0$	2.959×10^{-10}	2.842×10^{-6}	2.820×10^{-4}	1.007×10^{-2}
$Q=0.1$	3.296×10^{-10}	3.052×10^{-6}	3.003×10^{-4}	1.095×10^{-2}
$Q=0.3$	7.990×10^{-10}	5.498×10^{-6}	5.100×10^{-4}	2.382×10^{-2}
$Q=0.5$	5.383×10^{-9}	2.010×10^{-5}	1.774×10^{-3}	
$Q=0.7$	1.540×10^{-7}	2.292×10^{-4}	4.950×10^{-2}	
$Q=0.9$	1.290×10^{-4}			

Neumann	$z_c^{\max}(a=0.3)$	$z_c^{\max}(a=0.5)$	$z_c^{\max}(a=0.7)$	$z_c^{\max}(a=0.9)$
$Q=0$	6.455×10^{-6}	6.662×10^{-4}	7.417×10^{-3}	5.432×10^{-2}
$Q=0.1$	6.805×10^{-6}	6.902×10^{-4}	7.663×10^{-3}	5.693×10^{-2}
$Q=0.3$	1.050×10^{-5}	9.241×10^{-4}	1.009×10^{-2}	8.856×10^{-2}
$Q=0.5$	2.670×10^{-5}	1.762×10^{-3}	1.948×10^{-2}	
$Q=0.7$	1.372×10^{-4}	6.021×10^{-3}	1.247×10^{-1}	
$Q=0.9$	3.761×10^{-3}			

Table 4.1: Marginally-stable Kerr-Newman type ECOs with reflective Dirichlet or Neumann boundary conditions. For different angular momentum, a, and charge, Q, we present the largest dimensionless radius $z_c^{\max}$ of the horizonless ECO that can support the spatially regular static scalar field configurations for $l = m = 1$.

Analysing the results obtained in Table 4.1, for both boundary conditions, we observe that for a scalar mode $l = m = 1$ by fixing the angular momentum a, the critical radius $z_c^{\max}$ will increase monotonically when we increase the charge Q. If we fix instead the charge Q, by raising the angular momentum a, the critical radius $z_c^{\max}$ will also increase monotonically.

Dirichlet	$f(l=1)$	$f(l=2)$	$f(l=3)$	$f(l=4)$	$f(l=5)$
$Q=0$	9.330×10^{-1}	9.334×10^{-1}	9.347×10^{-1}	9.367×10^{-1}	9.390×10^{-1}
$Q=0.1$	9.325×10^{-1}	9.328×10^{-1}	9.342×10^{-1}	9.362×10^{-1}	9.385×10^{-1}
$Q=0.3$	9.276×10^{-1}	9.281×10^{-1}	9.297×10^{-1}	9.321×10^{-1}	9.348×10^{-1}
$Q=0.5$	9.149×10^{-1}	9.158×10^{-1}	9.184×10^{-1}	9.218×10^{-1}	9.253×10^{-1}
$Q=0.7$	8.811×10^{-1}	8.845×10^{-1}	8.906×10^{-1}	8.970×10^{-1}	9.030×10^{-1}

Neumann	$f(l=1)$	$f(l=2)$	$f(l=3)$	$f(l=4)$	$f(l=5)$
$Q=0$	9.336×10^{-1}	9.387×10^{-1}	9.448×10^{-1}	9.501×10^{-1}	9.544×10^{-1}
$Q=0.1$	9.331×10^{-1}	9.383×10^{-1}	9.445×10^{-1}	9.498×10^{-1}	9.542×10^{-1}
$Q=0.3$	9.284×10^{-1}	9.345×10^{-1}	9.413×10^{-1}	9.471×10^{-1}	9.518×10^{-1}
$Q=0.5$	9.164×10^{-1}	9.249×10^{-1}	9.335×10^{-1}	9.405×10^{-1}	9.460×10^{-1}
$Q=0.7$	8.862×10^{-1}	9.020×10^{-1}	9.152×10^{-1}	9.251×10^{-1}	9.327×10^{-1}

Table 4.2: Ratio between the largest surface critical radius $r_c^{\max}$ and the ergosurface radius $r_e(\pi/2)$. Here we fix the angular momentum $a = 0.5$ where we change the scalar field modes $l = m$ and the charge Q.

Now let us study the ratio between the largest critical radius for the Kerr-Newman-type ECO, $r_c^{\max}$ and the ergosurface radius for $\theta = \pi/2$, $r_e(\pi/2)$ (see (2.9)), that will be given by the parameter

$f = r_c^{\max}/r_e(\pi/2)$. In Table 4.2 we exhibit this ratio. Here we fix the ECO spin, $a = 0.5$, by changing the ECO charge and the scalar field configurations $l = m$.

We can observe that for a fixed charge the ratio f increases by increasing the equatorial modes $l = m$. This means that for a Kerr-Newman type ECO described by a specific spin a and charge Q, when we increase the equatorial modes $l = m$ the largest critical surface radius increases.

Another observation is the fact that the $r_c^{\max}$ is below the ergosurface radius $r_e(\pi/2)$ even if we increase the equatorial modes or the ECO charge. In others words, we can conclude that the superradiant instabilities in ECOs with $r_c < r_c^{\max}$ are due to the instabilities on the ergoregion.

4.2.2 Resonance spectra in the highly compact approximation

The resonance conditions equations (4.12) and (4.13) can be solved analytically in the small x_c regime ($x_c \ll 1$), which corresponds to the family of highly compact Kerr-Newman-type ECOs. For that let us use the property of Eq 15.3.6 of [32] in order to simplify the radial equation (4.11). Then, (4.11) can be expressed as

$$\begin{aligned} R(x) =& A\,\frac{(2l+1)!}{l!}(1-x)^{l+1}\left[\frac{\Gamma(2i\alpha)}{\Gamma(l+1+2i\alpha)}x^{-i\alpha}\,{}_2F_1(l+1-2i\alpha,l+1;1-2i\alpha;x)\right. \\ &\left.+\frac{\Gamma(-2i\alpha)}{\Gamma(l+1-2i\alpha)}x^{i\alpha}\,{}_2F_1(l+1+2i\alpha,l+1;1+2i\alpha;x)\right]. \end{aligned} \tag{4.14}$$

Imposing the property of the hypergeometric function when $x \to 0$, ${}_2F_1(a,b;c,x\to 0) \to 1$, (4.14), will be

$$R(x) \overset{x\to 0}{=} A\,\frac{(2l+1)!}{l!}(1-x)^{l+1}\left[\frac{\Gamma(2i\alpha)}{\Gamma(l+1+2i\alpha)}x^{-i\alpha}+\frac{\Gamma(-2i\alpha)}{\Gamma(l+1-2i\alpha)}x^{i\alpha}\right]. \tag{4.15}$$

Now we can apply the small-x behavior (4.15) into the boundary conditions (4.12) and (4.13). From the approximation we obtain two discrete sets, $\{x_c^{\rm D}(a,Q,l,m)_{n=1}^{n=\infty}\}$ and $\{x_c^{\rm N}(a,Q,l,m)_{n=1}^{n=\infty}\}$, each labelled by an integer number n, in a compact analytical formula, which take the form

$$x_c^{\rm D}(n) = e^{-\frac{\pi\left(n+\frac{1}{2}\right)}{\alpha}}\left[\frac{\Gamma(2i\alpha)\,\Gamma(l+1-2i\alpha)}{\Gamma(-2i\alpha)\,\Gamma(l+1+2i\alpha)}\right]^{\frac{1}{2i\alpha}}, \quad n\in\mathbb{N}, \tag{4.16}$$

for the Dirichlet boundary condition and

$$x_c^{\rm N}(n) = e^{-\frac{\pi n}{\alpha}}\left[\frac{\Gamma(2i\alpha)\,\Gamma(l+1-2i\alpha)}{\Gamma(-2i\alpha)\,\Gamma(l+1+2i\alpha)}\right]^{\frac{1}{2i\alpha}}, \quad n\in\mathbb{N}. \tag{4.17}$$

for the Neumann boundary condition.

Here we use the relation $e^{-2i\pi n} = 1$. Although this relation holds for $n \in \mathbb{Z}$ only for $n \in \mathbb{N}$ the resonance solutions of (4.16) and (4.17) are true solutions of (4.12) and (4.13). Moreover, it is not obvious that the expressions for $\{x_c^{\rm D}, x_c^{\rm N}\}$ in (4.16) and (4.17) are real numbers. To check that they are, we use Eq. 6.1.21 in [32] to find the relations $\Gamma(2i\alpha)/\Gamma(-2i\alpha) = e^{i\phi_1}$ and $\Gamma(l+1-2i\alpha)/\Gamma(l+1+2i\alpha) = e^{i\phi_2}$ where $\{\phi_1,\phi_2\} \in \mathbb{R}$. This implies that $\{x_c^{\rm D}, x_c^{\rm N}\} \in \mathbb{R}$.

With these discrete families of dimensionless critical radii which characterize the horizonless Kerr-Newman-type ECOs that can support the spatially regular static massless scalar field configurations, we can compare with the resonance spectra derived in (4.12) and (4.13). But first let us observe the resonance spectra by plotting (4.11).

In Fig.4.1 we have an illustrative representation of the resonance spectra relatively to the would-be horizon r_+ and the ergosurface radius $r_e(\pi/2)$ (top panel) and the radial profile of (4.11) for two different scales (down panel). From the radial profiles we observe the existence of the resonance solutions. Although it is not perceptive the existence of infinite resonance solutions in both radial profiles, if we zoom in consecutively for a lesser order on the radial profile (right panel) we will always observe resonance solutions, indicating the existence of infinite resonance solutions.

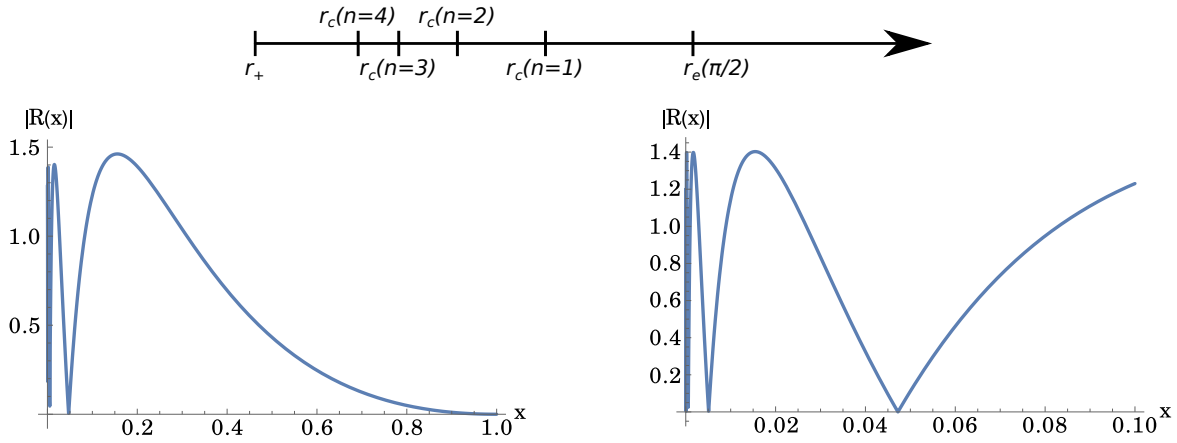

Figure 4.1: On the top panel we have an illustrative representation of the resonance solutions positions relatively to the would-be horizon r_+ and the ergosurface radius $r_e\,(\pi/2)$. On the down panel we have the Kerr-Newman-type ECO radial profile of (4.11) for $x \in [0,1]$ (left panel) and $x \in [0,0.1]$ (right panel). These last plots were obtained for $a = 0.9$, $Q = 0.3$, and $l = m = 1$.

Proceeding to the comparison, in Table 4.3 we present the values for the dimensionless radius z_c of the Kerr-Newman-type ECOs with reflecting Dirichlet or Neumann boundary conditions, respectively, where we compare the data obtained analytically through the compact expressions given by (4.16) and (4.17) with the data obtained numerically through the equations (4.12) and (4.13). In these tables we fix the angular momentum $a = 0.9$ for the massless scalar field mode $l = m = 1$ changing the charge Q.

Dirichlet		$z_c\,(n=1)$	$z_c\,(n=2)$	$z_c\,(n=3)$	$z_c\,(n=4)$
$Q = 0.1$	A	1.081×10^{-2}	5.495×10^{-4}	2.840×10^{-5}	1.469×10^{-6}
	N	1.095×10^{-2}	5.499×10^{-4}	2.840×10^{-5}	1.469×10^{-6}
	$E\,(\%)$	1.343	6.714×10^{-2}	3.467×10^{-3}	1.793×10^{-4}
$Q = 0.3$	A	2.329×10^{-2}	2.455×10^{-3}	2.687×10^{-4}	2.953×10^{-5}
	N	2.382×10^{-2}	2.461×10^{-3}	2.688×10^{-4}	2.953×10^{-5}
	$E\,(\%)$	2.236	2.257×10^{-1}	2.460×10^{-2}	2.702×10^{-3}

Neumann		$z_c\,(n=1)$	$z_c\,(n=2)$	$z_c\,(n=3)$	$z_c\,(n=4)$
$Q = 0.1$	A	5.064×10^{-2}	2.424×10^{-3}	1.249×10^{-4}	6.458×10^{-6}
	N	5.693×10^{-2}	2.434×10^{-3}	1.249×10^{-4}	6.458×10^{-6}
	$E\,(\%)$	11.04	4.313×10^{-1}	2.203×10^{-2}	1.139×10^{-3}
$Q = 0.3$	A	7.785×10^{-2}	7.481×10^{-3}	8.113×10^{-4}	8.908×10^{-5}
	N	8.856×10^{-2}	7.547×10^{-3}	8.121×10^{-4}	8.908×10^{-5}
	$E\,(\%)$	12.10	8.763×10^{-1}	9.281×10^{-2}	1.016×10^{-3}

Table 4.3: Kerr-Newman-type ECOs with reflective Dirichlet or Neumann boundary conditions. Here we compare the approximated radius z_c (analytical - A) with the exact radius solution (numerical - N) of the horizonless Kerr-Newman-type ECO by calculating the relative error, E (in %). Here we change the charge Q by fixing the angular momentum $a = 0.9$ and the equatorial mode $l = m = 1$.

We can see in Table 4.3, specially for $z_c \ll 1$, a good agreement between the approximated radius of the ECO and the exact radius solution. We also observe that the relative error, that is given by

$$\text{Relative Error}\,(\%) = \frac{|Numerical - Analytical|}{Numerical} \times 100, \tag{4.18}$$

decreases as we increase the value of n. All values obtained were approximated to four significant digits due to the size of the tables. For $Q = 0$ we observe the same results as obtained in [1].

4.3 Extremal Kerr

We now tackle the extremal case (which has not been, to the best of our knowledge discussed in the literature). But before considering the extremal Kerr-Newman type ECOs, let us study the simpler extremal Kerr-type ECO, that is with $Q = 0$ and $a = M$. In this case, the radial equation is given by (2.19) where $\mu = 0$, $q = 0$ and $Q = 0$. Also, the radial function will obey the same boundary conditions at the ECO surface radius, (4.2), and at the spatial infinity, (4.3).

To obtain the resonance spectra we have to impose the property (4.4), that we have seen in the previous section. Then the radial equation (2.19), for the extremal case, will take the form

$$\frac{d}{dr}\left(\left(r-M\right)^2\frac{dR\left(r\right)}{dr}\right)+\left\{\frac{M^2m^2}{\left(r-M\right)^2}-l\left(l+1\right)\right\}R\left(r\right)=0. \tag{4.19}$$

We observe that the radial equation for a static scalar field is much simpler in the extremal case than for the sub-extremal regime. To solve (4.19), we will proceed in a different way. First, we want to get rid of the first derivative terms that come from the first term. For that we redefine the dependent variable $R\left(r\right)\rightarrow W\left(r\right)$ where

$$R\left(r\right)=\frac{M}{r-M}W\left(r\right). \tag{4.20}$$

Second we change the independent variable. Here we rescale the spacetime coordinate $r\in[M,+\infty[$ to $z\in[0,+\infty[$ by changing

$$z=\frac{r-M}{M}. \tag{4.21}$$

Note that the new variable z is the same as (4.1) in the extremal regime and will be the variable used for the construction of the resonance spectra. Performing these transformations, (4.20) and (4.21), into the radial equation (4.19) we have

$$z^2\frac{d^2W_{lm}\left(z\right)}{dz^2}+\left\{\frac{m^2}{z^2}-l\left(l+1\right)\right\}W_{lm}\left(z\right)=0. \tag{4.22}$$

If we solve the equation (4.22), we obtain as solutions the Bessel functions of the first kind, $J_\nu\left(x\right)$. To obtain the equation in a more canonical form of the Bessel equation, we change again the independent variable z to

$$y=\frac{m}{z}. \tag{4.23}$$

Changing this new variable, the radial equation will take the form of a well known differential equation - the spherical Bessel equation (see Eq. 10.1.1 of [32]). Then the radial equation (4.22) takes the form

$$y^2\frac{d^2W\left(y\right)}{dz^2}+2y\frac{dW\left(y\right)}{dz}+\left[y^2-l\left(l+1\right)\right]W\left(y\right)=0, \tag{4.24}$$

which solution is given by a linear combination of the spherical Bessel function of the first kind, $j_\nu\left(x\right)$, and the spherical Bessel function of the second kind, $y_\nu\left(x\right)$.

The radial function in terms of $R\left(z\right)$ will be

$$R\left(z\right)=\frac{1}{z}\left[C\,j_l\left(\frac{m}{z}\right)+D\,y_l\left(\frac{m}{z}\right)\right], \tag{4.25}$$

where C and D are normalization constants.

Having obtained the solution for the extremal Kerr-type ECO, let us impose boundary conditions. As we have seen in the previous section, the radial eigenfunction should vanish at spatial infinity, see

(4.3). So, for $r \to \infty$, the new variable will also be as $z \to \infty$. Then the radial equation (4.25), near spatial infinity approximates to

$$R(z) \overset{z\to\infty}{=} \left[C \, \frac{m^l}{z^{l+1}} \frac{1}{(2l+1)!!} - D \, \frac{z^l}{m^{l+1}} (2l+1)!! \right] . \tag{4.26}$$

To obey the asymptotic behavior (4.3), we require that the normalization constant D is zero and the radial equation is now

$$R(z) = C \frac{1}{z} j_l \left(\frac{m}{z} \right) . \tag{4.27}$$

By plotting the solution of the radial equation (4.27) we can clearly see the infinite resonance conditions (see Fig.4.2).

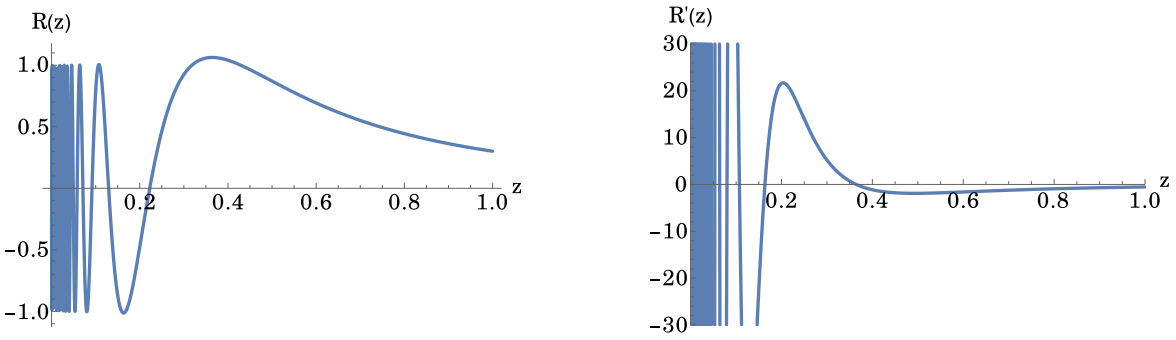

Figure 4.2: Radial profile of the extremal Kerr-type ECO (left panel) and its derivative (right panel). Here we set $l = m = 1$.

At last we impose the reflective boundary conditions (4.2), and we obtain a set of resonance equations for each boundary conditions that will be given as

$$\begin{cases} j_l \left(\frac{m}{z_c} \right) = 0 & \text{, for Dirichlet B.C. ,} \\ \frac{d}{dz} \left[\frac{1}{z} j_l \left(\frac{m}{z} \right) \right] \Big|_{z=z_c} = 0 & \text{, for Neumann B.C .} \end{cases} \tag{4.28}$$

4.3.1 Resonance spectra

With the resonance equations given by in (4.28) we can now construct the discrete set of surface radii, $\{r_c(l,m;n)_{n=1}^{n=\infty}\}$ for each reflective boundary condition in which the extremal Kerr-type ECO supports static massless scalar field configurations. In here we will determine the outermost dimensionless critical radius that marks the boundary between stable and unstable extremal Kerr-type ECOs.

Another thing that we will study is the transition between the results obtained in [1] for the Kerr spacetime and our results for the extremal case. Here we approximate the value of a to 1, where we reproduce numerically the results of [1], and see if it converges to our numerical result.

In Fig 4.3 it is represented that convergence. We observe that for $a \to 1$, calculated by the resonance conditions in [1], the critical radius tends to the value obtained by the conditions (4.28). This means that for $a \to 1$ the hypergeometric function tends to behave like a spherical Bessel function of the first kind. Also we observe an increase for $z_c^{\max}$ in this transition for both resonance conditions.

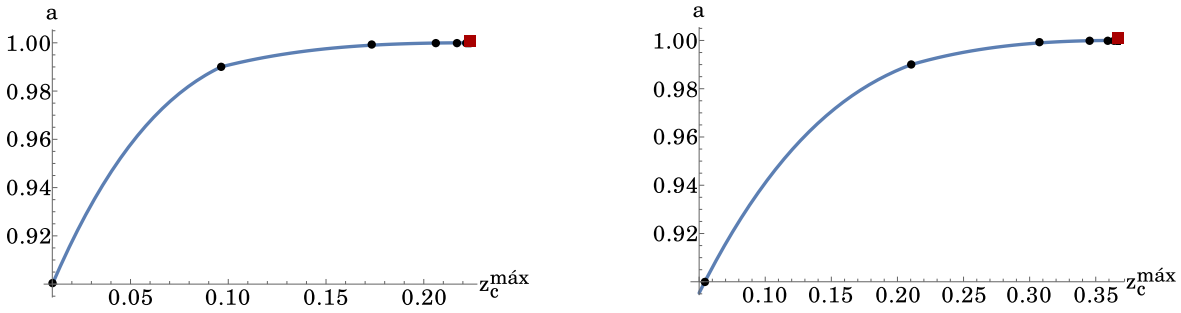

Figure 4.3: Convergence of the largest dimensionless critical surface radius $z_c^{\max}$, that corresponds to the transition between the results obtained in [1] for $a \to 1$ and our results for $a = 1$ obtained with the Dirichlet resonance condition (left panel) and Neumann resonance condition (right panel). The data (black dots) obtained by the resonance conditions of [1] clearly converges to our numerical value (red square). The values were obtained for $l = m = 1$.

In this case, the discrete family of critical surface radii only depends on the harmonic indices $\{l, m\}$, of the scalar field. So for various values of the equatorial modes, $l = m$, we present in Table 4.4 the outermost dimensionless surface radius $z_c^{\max}$ of the extremal Kerr-type ECO that supports static (marginally-stable) scalar field configurations.

	$z_c^{\max}\,(l=1)$	$z_c^{\max}\,(l=2)$	$z_c^{\max}\,(l=3)$	$z_c^{\max}\,(l=4)$	$z_c^{\max}\,(l=5)$
Dirichlet	2.225×10^{-1}	3.470×10^{-1}	4.293×10^{-1}	4.888×10^{-1}	5.344×10^{-1}
Neumann	3.645×10^{-1}	5.168×10^{-1}	6.032×10^{-1}	6.599×10^{-1}	7.002×10^{-1}

Table 4.4: Marginally-stable extremal Kerr-type ECO with reflective Dirichlet or Neumann boundary conditions. Here we present $z_c^{\max}$ of the horizonless extremal Kerr-type ECO that supports static equatorial, $l = m$, scalar field configurations.

We observe, from Table 4.4, the same behavior as obtained for the sub-extremal regime: $z_c^{\max}$ increases monotonically as we increase the harmonic index l.

4.3.2 Resonance spectra in the highly compact approximation

Now let us perform an approximation for $z_c \ll 1$ in the resonance equations (4.28). As we have mentioned before, in this regime we have the family of highly compact ECOs and if we perform an approximation to the resonance equations (4.28) we obtain a compact formula for each resonance solution. So for $z \to 0$ the radial equation (4.27) behaves as

$$R\left(z\right) \overset{z\to 0}{=} C\frac{1}{m}\sin\left(\frac{m}{z}-\frac{l\pi}{2}\right). \tag{4.29}$$

If we impose the reflective boundary conditions (4.2), we obtain two discrete sets, $\{z_c^{\mathrm{D}}\left(l,m;n\right)_{n=1}^{n=\infty}\}$ and $\{z_c^{\mathrm{N}}\left(l,m;n\right)_{n=1}^{n=\infty}\}$, where we have a compact formula for the first

$$z_c^{\mathrm{D}}\left(n\right) = \frac{m}{\pi\left(\frac{l}{2}+n\right)}, \quad n \in \mathbb{N} \tag{4.30}$$

and for the latter

$$z_c^{\mathrm{N}}\left(n\right) = \frac{m}{\pi\left(\frac{l}{2}-\frac{1}{2}+n\right)}, \quad n \in \mathbb{N}. \tag{4.31}$$

From these expressions we can find an analytical approximation for the discrete set obtained by (4.28). In Table 4.5 we present the dimensionless critical surface radius z_c of the analytical compact

formulas (4.30) and (4.31), and for the numerically resonance equation (4.28). There we compare the results obtained analytically and numerically through the relative error, given by (4.18), for the equatorial mode $l = m = 1$.

		$z_c\,(n=1)$	$z_c\,(n=2)$	$z_c\,(n=3)$	$z_c\,(n=4)$	$z_c\,(n=5)$
Dirichlet	A	2.122×10^{-1}	1.273×10^{-1}	9.092×10^{-2}	7.074×10^{-2}	5.787×10^{-2}
	N	2.225×10^{-1}	1.294×10^{-1}	9.171×10^{-2}	7.109×10^{-2}	5.807×10^{-2}
	$E\,(\%)$	4.647	1.639	8.317×10^{-1}	5.020×10^{-1}	3.357×10^{-1}
Neumann	A	3.183×10^{-1}	1.592×10^{-1}	1.061×10^{-1}	7.958×10^{-2}	6.366×10^{-2}
	N	3.645×10^{-1}	1.635×10^{-1}	1.073×10^{-1}	8.009×10^{-2}	6.392×10^{-2}
	$E\,(\%)$	12.67	2.649	1.148	6.401×10^{-1}	4.081×10^{-1}

Table 4.5: Extremal Kerr-type ECOs with reflective Dirichlet or Neumann boundary conditions. Here we compare the approximated radius z_c (analytical - A) with the exact radius solution (numerical - N) of the horizonless extremal Kerr-type ECO by calculating the relative error, E (in %). The values where obtained for $l = m = 1$.

We observe, from Table 4.5, that as we increase the value of n, the analytical dimensionless radius approximates with a good precision to the exact dimensionless radius, as we can see from the relative error. This means that we have a good agreement between the analytical resonance equations and the numerical resonance equations.

4.4 Extremal Kerr-Newman

We now generalize the previous subsection to extremal Kerr-Newman-type ECOs. The radial equation will be similar to the one for the Kerr-like ECO, but we now have $M = \sqrt{a^2 + Q^2}$ instead of $a = M$. So the radial equation will be

$$\frac{d}{dr}\left((r-M)^2 \frac{dR_{lm}(r)}{dr}\right) + \left\{\frac{a^2m^2}{(r-M)^2} - l(l+1)\right\} R_{lm}(r) = 0. \tag{4.32}$$

Performing the same transformations made in the previous section, see (4.20), (4.21) and (4.23), the solution will again be given as a linear combination of spherical Bessel functions that takes the form of

$$R(z) = \frac{1}{z}\left[E\, j_l\left(\frac{am}{z}\right) + F\, y_l\left(\frac{am}{z}\right)\right], \tag{4.33}$$

where E and F are normalization constants.

By imposing the boundary condition at spatial infinity (4.3), the radial equation (4.33) reduces to

$$R(z) = E\frac{1}{z} j_l\left(\frac{am}{z}\right). \tag{4.34}$$

If we plot (4.34) we observe the same behavior as in Fig.4.2 .

The reflective boundary conditions will now be given by

$$\begin{cases} j_l\left(\frac{am}{z}\right) = 0 & , \quad \text{for Dirichlet B.C. ,} \\ \frac{d}{dz}\left[\frac{1}{z} j_l\left(\frac{am}{z}\right)\right]\Big|_{z=z_c} = 0 & , \quad \text{for Neumann B.C. ,} \end{cases} \tag{4.35}$$

where the extremal Kerr-Newman-type ECO supports static scalar field configurations.

4.4.1 Resonance spectra

From the resonance equations (4.35), we can now construct the discrete set of critical surface radii $\{r_c(a, Q, l, m; n)_{n=1}^{n=\infty}\}$ where the extremal Kerr-Newman-type ECO can support static (marginally-stable) scalar field configurations. First we study the convergence between the resonance conditions (4.12)-(4.13) and (4.35) when we approach $a^2 + Q^2 \to 1$ - see Fig.4.4 .

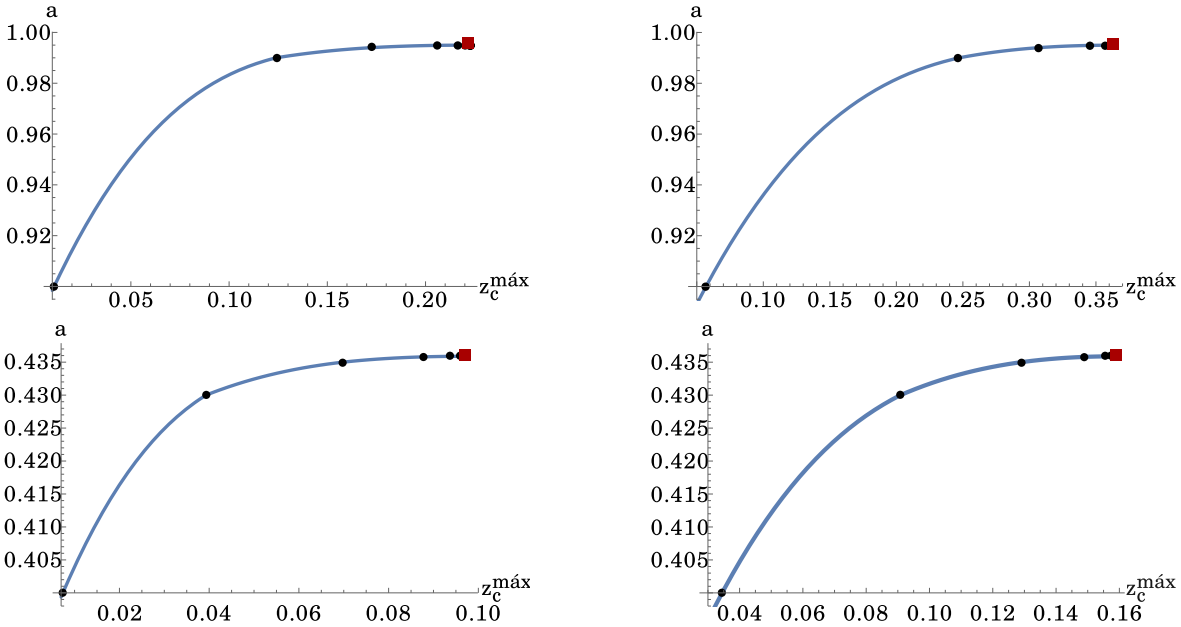

Figure 4.4: Convergence of the largest dimensionless critical surface radius $z_c^{\max}$, that corresponds to the transition between the results obtained (4.12) and (4.13) when $a \to \sqrt{1-Q^2}$ and (4.35) for $a = \sqrt{1-Q^2}$, obtained with the Dirichlet resonance condition (two plots in the left panel) and Neumann resonance condition (two plots in the right panel). The data (black dots) obtained by the resonance conditions (4.12) and (4.13) clearly converges to the values of (4.35) (red square). The values were obtained for $l = m = 1$ and for two different values of Q: $Q = 0.1$ (the two plots in the top panel) and $Q = 0.9$ (the two plots in the down panel).

We observe, from Fig.4.4, that for $a^2 + Q^2 \to 1$, where we change the charge Q for two different values ($Q = 0.1$ and $Q = 0.9$), the $z_c^{\max}$ obtained by the resonance equations (4.12) and (4.13) will tend to $z_c^{\max}$ obtained by the resonance equations (4.35). Concluding that the hypergeometric function for $a^2 + Q^2 \to 1$ will behave like the spherical Bessel function of the first kind. This is valid for all values of Q.

Now let us study the behavior for a fixed charge Q - which consequently means a fixed angular momentum a - by changing the harmonic indices $\{l, m\}$ assuming equatorial modes $l = m$. In Table 4.6 we show $z_c^{\max}$ that characterizes the extremal Kerr-Newman-type ECO that can support static (marginally-stable) scalar field configurations, for various equatorial modes, $l = m$, where we choose to fix $Q = 0.9$.

	$z_c^{\max}\,(l=1)$	$z_c^{\max}\,(l=2)$	$z_c^{\max}\,(l=3)$	$z_c^{\max}\,(l=4)$	$z_c^{\max}\,(l=5)$
Dirichlet	9.701×10^{-2}	1.513×10^{-1}	1.871×10^{-1}	2.131×10^{-1}	2.330×10^{-1}
Neumann	1.589×10^{-1}	2.253×10^{-1}	2.629×10^{-1}	2.876×10^{-1}	3.052×10^{-1}

Table 4.6: Marginally-stable extremal Kerr-Newman-type ECO with reflective Dirichlet or Neumann boundary condition. Here we present $z_c^{\max}$ of the horizonless extremal Kerr-Newman-type ECO for $Q = 0.9$ that supports static equatorial, $l = m$, scalar field configurations.

Observing Table 4.6, for a fixed value of charge $Q = 0.9$, the dimensionless critical surface radius $z_c^{\max}$ increases monotonically when we increase the equatorial mode, keeping the same behavior as the extremal Kerr-type ECO.

4.4.2 Resonance spectra in the highly compact approximation

Now let us perform an approximation for the small regime $z_c \ll 1$ in the resonances conditions (4.35) that correspond to the family of highly compact extremal Kerr-Newman-type ECOs. Considering this regime, (4.34) will now behave as

$$R(z) \overset{z\to 0}{=} E\frac{1}{am}\sin\left(\frac{am}{z}-\frac{l\pi}{2}\right). \tag{4.36}$$

Imposing the reflective boundary conditions (4.2), we obtain two discrete sets for $\{z_c^{\mathrm{D}}(a,l,m;n)_{n=1}^{n=\infty}\}$ and for $\{z_c^{\mathrm{N}}(a,l,m;n)_{n=1}^{n=\infty}\}$, where the compact formulas are given by

$$z_c^{\mathrm{D}}(n) = \frac{am}{\pi\left(\frac{l}{2}+n\right)}, \quad n\in\mathbb{N}, \tag{4.37}$$

and

$$z_c^{\mathrm{N}}(n) = \frac{am}{\pi\left(\frac{l}{2}-\frac{1}{2}+n\right)}, \quad n\in\mathbb{N}\,, \tag{4.38}$$

respectively.

In Table 4.7 we display the dimensionless critical surface radius z_c of the analytical compact formulas (4.37) and (4.38), and the numerically resonance conditions (4.35). Again, we compare the results obtained analytically and numerically through the relative error, given by (4.18), for the equatorial mode $l=m=1$ and $Q=0.1$.

		$z_c\,(n=1)$	$z_c\,(n=2)$	$z_c\,(n=3)$	$z_c\,(n=4)$	$z_c\,(n=5)$
Dirichlet	A	2.111×10^{-1}	1.267×10^{-1}	9.049×10^{-2}	7.038×10^{-2}	5.758×10^{-2}
	N	2.214×10^{-1}	1.288×10^{-1}	9.125×10^{-2}	7.074×10^{-2}	5.778×10^{-2}
	$E\,(\%)$	4.647	1.639	8.317×10^{-1}	5.020×10^{-1}	3.357×10^{-1}
Neumann	A	3.167×10^{-1}	1.584×10^{-1}	1.056×10^{-1}	7.918×10^{-2}	6.334×10^{-2}
	N	3.626×10^{-1}	1.627×10^{-1}	1.068×10^{-1}	7.969×10^{-2}	6.360×10^{-2}
	$E\,(\%)$	12.67	2.649	1.148	6.401×10^{-1}	4.081×10^{-1}

Table 4.7: Extremal Kerr-type ECOs with reflective Dirichlet or Neumann boundary conditions. Here we compare the approximated radius z_c (analytical - A) with the exact radius solution (numerical - N) of the horizonless extremal Kerr-Newman-type ECO by calculating the relative error, E (in %). The values where obtained for $l=m=1$ and for $Q=0.1$.

From Table 4.7, we observe for both boundary conditions, a good agreement between the approximated dimensionless radius obtained by (4.37) and (4.38) and the exact dimensionless radius solution obtained by (4.35). This is observed by the relative error where the maximum value for the Dirichlet boundary condition is $\sim 4.6\%$ whereas for the Neumann boundary condition is $\sim 12.7\%$. Also the relative error decreases when we increase the parameter n.

4.5 Super-extremal Kerr-Newman

In the previous sections we solved the system analytically for horizonless ECOs in the sub-extremal regime $\left(M>\sqrt{a^2+Q^2}\right)$ and in the extremal regime $\left(M=\sqrt{a^2+Q^2}\right)$. But are there analytical solutions for the super-extremal regime $\left(M<\sqrt{a^2+Q^2}\right)$? In fact there are and differently from the previous cases the resonance spectra is composed of a finite number of solutions. These analytical solutions were presented by [3] for a Kerr-type ECO with reflective properties.

Following the same process as in [3], we will obtain the discrete family set of critical radius $\{r_c(a,Q,l,m;n)_{n=1}^{n=N}\}$ of the super-extremal Kerr-Newman-type ECO that can support (marginally-stable) static scalar field configurations.

Now let us impose the property (4.4) into the radial differential equation (2.19) for $\mu = 0$ and $q = 0$. Here we obtain the same radial differential equation (4.5) as obtained in the sub-extremal regime which solutions are given by the radial equation (4.9). However, due to the condition $M < \sqrt{a^2 + Q^2}$, we will have an imaginary factor in the quantities $r_\pm$ ($r_\pm = M \pm i\sqrt{a^2 + Q^2 - M^2}$). So the radial equation (4.9) can be written as

$$\begin{aligned} R(x) =& x^{-\frac{\xi}{2}} (1-x)^{l+1} \left\{ A \ {}_2F_1(l+1-\xi, l+1; 2l+2; 1-x) \right. \\ &\left. + B (1-x)^{-2l-1} \ {}_2F_1(-l-\xi, -l; -2l; 1-x) \right\}, \end{aligned} \tag{4.39}$$

where $\xi = 2i\alpha$ and $x \in \mathbb{C}$ (see (4.7)).

Imposing the boundary conditions at spatial infinity (4.3) the only physical acceptable solution is when $B = 0$, as we have seen before, so the radial equation (4.39) simplifies to

$$R(x) = A x^{-\frac{\xi}{2}} (1-x)^{l+1} \ {}_2F_1(l+1-\xi, l+1; 2l+2; 1-x) \,. \tag{4.40}$$

At last we impose the reflective boundary conditions and one obtain the following compact resonance conditions:

$${}_2F_1(l+1-\xi, l+1; 2l+2; 1-x_c) = 0, \tag{4.41}$$

for the Dirichlet boundary condition and

$$\frac{d}{dx}\left[x^{-\frac{\xi}{2}} (1-x)^{l+1} \ {}_2F_1(l+1-\xi, l+1; 2l+2; 1-x) \right]_{x=x_c} = 0, \tag{4.42}$$

for the Neumann boundary condition.

Before presenting the resonance spectra, there are some properties about the radial equation (4.40) that are very important to mention. First is the fact that the radial equation (4.40) is symmetric for $r = M$. To prove, let us change the complex independent variable x by the real parameter z that is given by (4.21). If we substitute $x \to z$ and use the hypergeometric identity Eq. 15.3.15 of [32] into (4.40) we obtain the following equation,

$$R(z) = A \left(\frac{-4\left(a^2+Q^2-1\right)}{z^2+a^2+Q^2-1} \right)^{\frac{l+1}{2}} {}_2F_1\left(\tfrac{1}{2}(l+1-\xi), \tfrac{1}{2}(l+1-\xi); l+\tfrac{3}{2}; \tfrac{a^2+Q^2-1}{z^2+a^2+Q^2-1} \right). \tag{4.43}$$

By plotting (4.43), see Fig. 4.5, we observe that the radial equation is invariant under reflections of $z \to -z$ and, by analisyng (4.43), it is also invariant under reflections of $m \to -m$.

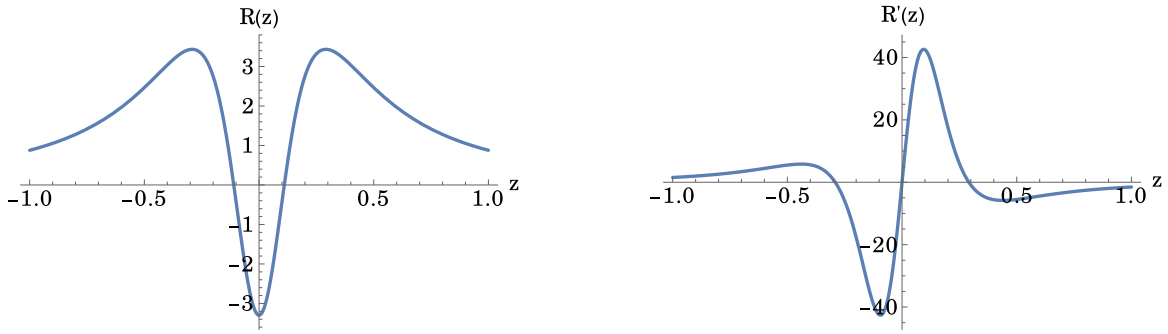

Figure 4.5: Radial profile of (4.43) (left panel) and its derivative (right panel) for $Q = 0.3$, $a \simeq 0.985$ and $l = m = 1$.

So if we impose the reflective boundary conditions, we observe two things. First, if the dimensionless surface radius z_c is a solution of the resonance conditions, then $-z_c$ is also a valid solution. Second, if the z_c characterizes the super-extremal Kerr-Newman-type ECO with $m > 0$ then the same

dimensionless radius characterizes the super-extremal Kerr-Newman type ECO with $m < 0$. Thus we can assume, without loss of generality, $m > 0$ and $z_c \geq 0$.

Another property of (4.40) is the existence of finite solutions. This can be observed by changing the parameter $l+1-\xi$ in the hypergeometric function where the number of solutions for the Dirichlet boundary condition, (4.41), is given by

$$N_d = \begin{cases} \xi - (l+1) & \text{if } \xi - (l+1) \text{ is a positive integer;} \\ \lfloor \xi - (l+1) \rfloor & \text{if } \lfloor \xi - (l+1) \rfloor \text{ is a positive even integer;} \\ \lfloor \xi - (l+1) \rfloor + 1 & \text{if } \lfloor \xi - (l+1) \rfloor \text{ is a positive odd integer;} \end{cases} \tag{4.44}$$

while for the Neumann boundary condition is

$$N_n = \begin{cases} \xi - (l+1) + 1 & \text{if } \xi - (l+1) \text{ is a positive integer;} \\ \lfloor \xi - (l+1) \rfloor + 2 & \text{if } \lfloor \xi - (l+1) \rfloor \text{ is a positive even integer;} \\ \lfloor \xi - (l+1) \rfloor + 1 & \text{if } \lfloor \xi - (l+1) \rfloor \text{ is a positive odd integer.} \end{cases} \tag{4.45}$$

Here the parenthesis $\lfloor h \rfloor$ corresponds to the greatest integer less than or equal to h. In Fig.4.6 we observe the finite resonance solutions when we change the scalar field modes.

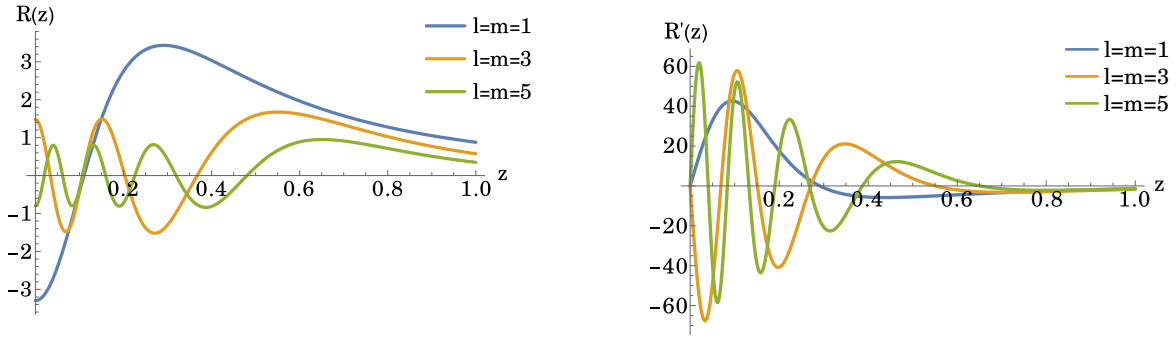

Figure 4.6: Radial profile of the super-extremal Kerr-Newman type ECO (left panel) and its derivative (right panel). Here we set $Q = 0.3$ and $a \simeq 0.985$ by changing the scalar modes $l = m$.

With these properties in mind we can construct more easily the resonance spectra of the super-extremal Kerr-Newman-type ECO that supports static (marginally-stable) massless scalar field configurations.

4.5.1 Regime of existence

To fully describe the composed super-extremal Kerr-Newman-type ECO it is necessary to determine the upper bound on the characteristic surface radius $\{r_c\,(a, Q, l, m; n)_{n=1}^{n=N}\}$ where is possible the existence of the system. Let us introduce a new scalar function

$$U\,(r) \equiv \Delta^{\frac{1}{2}} R\,(r)\,. \tag{4.46}$$

Substituting into (4.5), one obtain a simple differential ordinary equation

$$\Delta^2 \frac{d^2 U\,(r)}{dr^2} + \left[m^2 a^2 - l\,(l+1)\,\Delta - \left(a^2 + Q^2 - 1\right)\right] U\,(r) = 0. \tag{4.47}$$

Knowing that at the surface radius r_c and at spatial infinity $r \to \infty$ the radial equation should vanish, the scalar function $U\,(r)$ should have at least one extremum point at $r = r_p$ in the interval $[r_c, \infty[$. Then the scalar function obeys the same relations as we have seen in Chapter 3 when we

established the no-hair theorem for ECOs, see (3.8). From these relations we can obtain the following inequality

$$m^2a^2 - l\left(l+1\right)\left(r_p^2 - 2r_p + a^2 + Q^2\right) - \left(a^2 + Q^2 - 1\right) > 0. \tag{4.48}$$

This inequality implies that $r_p \in]r_{p-}, r_{p+}[$ where

$$r_{p\pm} = 1 \pm \sqrt{1 - \frac{a^2\left[1 + l\left(l+1\right) - m^2\right] + Q^2\left[1 + l\left(l+1\right)\right] - 1}{l\left(l+1\right)}}. \tag{4.49}$$

By taking in consideration these relations and (4.21), we can deduce that the super-extremal Kerr-Newman-type ECO is characterized by the upper bound

$$|z_c| < \sqrt{1 - \frac{a^2\left[1 + l\left(l+1\right) - m^2\right] + Q^2\left[1 + l\left(l+1\right)\right] - 1}{l\left(l+1\right)}}. \tag{4.50}$$

In addition to this upper bound, we observe that $a^2\left[1 + l\left(l+1\right) - m^2\right] + Q^2\left[1 + l\left(l+1\right)\right] - 1 \leq l\left(l+1\right)$. Then we can calculate the possible range of values for the angular momentum a, that will be bounded by

$$\sqrt{1-Q^2} < a < \sqrt{\frac{\left(1-Q^2\right)\left[1 + l\left(l+1\right)\right]}{l\left(l+1\right) + 1 - m^2}}. \tag{4.51}$$

In [3] a stronger upper bound for a was obtained due to the behavior of the hypergeometric function where it was found that

$${}_2F_1\left(l+1-\xi, l+1; 2l+2; 1-x\right) \neq 0 \quad \text{for} \quad \{r \in \mathbb{R} \text{ and } -1 < l+1-\xi < 2l+3\}. \tag{4.52}$$

However, if $l+1-\xi = -1$ or $l+1-\xi = 2l+3$, the hypergeometric starts to admit zeros. In our case it was also possible to observe this behavior, which permits to calculate the following stronger upper bound

$$\sqrt{1-Q^2} < a \leq \sqrt{\frac{\left(1-Q^2\right)\left(l+2\right)^2}{\left(l+2\right)^2 - m^2}}, \tag{4.53}$$

for the ECO spin. Here the equality sign corresponds to the super-extremal Kerr-Newman-type ECO with $r_c = M$ (or $z = 0$).

4.5.2 Resonance spectra

By establishing the regime of existence of the system and knowing its properties we can now construct the resonance spectra for the Dirichlet boundary condition ,$\{r_c\left(a, Q, l, m; n\right)_{n=1}^{n=N_d}\}$, and for the Neumann boundary condition ,$\{r_c\left(a, Q, l, m; n\right)_{n=1}^{n=N_n}\}$ which characterizes the super-extremal Kerr-Newman-type ECO that supports static (marginally-stable) scalar configurations.

Before proceeding to the results let us introduce the new parameter b that will help us to construct the resonance spectra. This parameter is in the range of $b \in]0, b_{\max}]$ (where $b_{\max} = m/\left(l+2\right)$) and, according to (4.53), it is related to the angular momentum by the expression

$$a = \sqrt{\frac{1-Q^2}{1-b^2}}. \tag{4.54}$$

Now we can finally proceed to the results. In Table 4.8 we present the smallest and the largest dimensionless surface radius z_c for the Dirichlet or Neumann boundary conditions. Here we change the parameter b according to its range of values and the charge Q for two different values ($Q = 0.1$ and $Q = 0.9$) by fixing the equatorial modes at $l = m = 1$. Also the number of resonance solutions is displayed.

(a) Dirichlet for $Q = 0.1$

b	N_d	$z_c^{\min}$	$z_c^{\max}$
$b_{\max}$	1	0.0	0.0
0.30	2	5.461×10^{-2}	5.461×10^{-2}
0.25	2	1.149×10^{-1}	1.149×10^{-1}
0.20	3	0.0	1.573×10^{-1}
0.15	4	6.423×10^{-2}	1.869×10^{-1}
0.10	8	1.600×10^{-2}	2.066×10^{-1}
0.05	18	3.930×10^{-3}	2.178×10^{-1}

(b) Neumann for $Q = 0.1$

b	N_n	$z_c^{\min}$	$z_c^{\max}$
$b_{\max}$	2	2.488×10^{-1}	2.488×10^{-1}
0.30	2	2.740×10^{-1}	2.740×10^{-1}
0.25	3	0.0	3.040×10^{-1}
0.20	4	6.920×10^{-2}	3.265×10^{-1}
0.15	6	2.449×10^{-2}	3.429×10^{-1}
0.10	9	0.0	3.540×10^{-1}
0.05	19	0.0	3.605×10^{-1}

(c) Dirichlet for $Q = 0.9$

b	N_d	$z_c^{\min}$	$z_c^{\max}$
$b_{\max}$	1	0.0	0.0
0.30	2	2.392×10^{-2}	2.392×10^{-2}
0.25	2	5.033×10^{-2}	5.033×10^{-2}
0.20	3	0.0	6.892×10^{-2}
0.15	4	2.814×10^{-2}	8.189×10^{-2}
0.10	8	7.010×10^{-3}	9.049×10^{-2}
0.05	18	1.722×10^{-3}	9.541×10^{-2}

(d) Neumann for $Q = 0.9$

b	N_n	$z_c^{\min}$	$z_c^{\max}$
$b_{\max}$	2	1.090×10^{-1}	1.090×10^{-1}
0.30	2	1.200×10^{-1}	1.200×10^{-1}
0.25	3	0.0	1.332×10^{-1}
0.20	4	3.032×10^{-2}	1.430×10^{-1}
0.15	6	1.073×10^{-2}	1.502×10^{-1}
0.10	9	0.0	1.551×10^{-1}
0.05	19	0.0	1.579×10^{-1}

Table 4.8: Marginally-stable super-extremal Kerr-Newman-type ECOs with reflective Dirichlet or Neumann boundary conditions. For different values of b, and two different charges, $Q = 0.1$ (4.8a and 4.8b) and $Q = 0.9$ (4.8c and 4.8d), we present $z_c^{\min}$ and $z_c^{\max}$ of the horizonless ECO that can support spatially regular static scalar field configurations $l = m = 1$. Also the number of resonance solutions is displayed.

From Table 4.8 we observe that for a fixed value of Q, the largest dimensionless surface radius $z_c^{\max}$, for both boundary conditions, increases as we decrease the parameter b, *i.e.* according to (4.54), as we decrease a. Also by decreasing b the number of resonance solutions increases. If we compare between the two values of Q we observe that for a fixed b, the smallest and the largest dimensionless surface radius z_c will decrease as we increase the charge Q.

Now let us proceed to study the behavior of z_c for various equatorial modes, $l = m$, displayed in Table 4.9. Here we fix $b = 0.25$ and $Q = 0.9$.

(a) Dirichlet

$l = m$	N_d	$z_c^{\min}$	$z_c^{\max}$
1	2	5.033×10^{-2}	5.033×10^{-2}
2	5	0.0	1.251×10^{-1}
3	8	1.549×10^{-2}	1.678×10^{-1}
4	11	0.0	1.973×10^{-1}
5	14	9.212×10^{-3}	2.194×10^{-1}
6	17	0.0	2.369×10^{-1}

(b) Neumann

$l = m$	N_n	$z_c^{\min}$	$z_c^{\max}$
1	3	0.0	1.332×10^{-1}
2	6	2.358×10^{-2}	2.101×10^{-1}
3	9	0.0	2.517×10^{-1}
4	12	1.155×10^{-2}	2.785×10^{-1}
5	15	0.0	2.975×10^{-1}
6	19	7.622×10^{-3}	3.118×10^{-1}

Table 4.9: Marginally-stable super-extremal Kerr-Newman-type ECO with reflective Dirichlet or Neumann boundary condition. Here we present $z_c^{\min}$ and $z_c^{\max}$ of the horizonless super-extremal Kerr-Newman-type ECO for $Q = 0.9$ that supports static equatorial, $l = m$, scalar field configurations. Also the number of resonance solutions is displayed.

We observe, from Table 4.9, that the largest dimensionless surface radius, $z_c^{\max}$, for both reflective boundary condition, increases as we increase the equatorial modes $l = m$. Also by increasing $l = m$ the number of resonance solutions increases. This is valid for all values of Q.

All results obtained are in agreement with the data obtained in [3] for $Q = 0$. Furthermore the

results satisfy the upper bound (4.50).

4.5.3 Resonance spectra for near-critical approximation

In this section we present a compact resonance formula of (4.41) and (4.42) for the near-critical regime $0 < a^2 + Q^2 - 1 \ll 1$. In this regime we observe from (4.40) that $\xi \gg l$ permitting to use the following asymptotic expansion, see [3],

$$ {}_2F_1\left(a, b; c; z\right) = \frac{\Gamma\left(c\right)}{\Gamma\left(c-a\right)}\left(-bz\right)^{-a}\left[1 + O\left(|bz|^{-1}\right)\right] + \frac{\Gamma\left(c\right)}{\Gamma\left(a\right)}\left(bz\right)^{a-c}\left(1-z\right)\left[1 + O\left(|bz|^{-1}\right)\right], \quad (4.55) $$

when $|b|$ is large.

Using (4.55) into (4.41) and (4.42) and changing x to z, see (4.7) and (4.21) respectively, we obtain two discrete sets $\{z_c^{\mathrm{D}}\left(a, Q, l, m; n\right)_{n=1}^{n=N_d}\}$ and $\{z_c^{\mathrm{N}}\left(a, Q, l, m; n\right)_{n=1}^{n=N_n}\}$, where we have a compact formula for the former

$$ z_c^{\mathrm{D}}\left(n\right) = \sqrt{a^2+Q^2-1}\ \cot\left(\frac{\pi\left(l+2n\right)}{2\xi}\right) \quad \text{with} \quad n \in \mathbb{N}, \quad (4.56) $$

and for the latter

$$ z_c^{\mathrm{N}}\left(n\right) = \sqrt{a^2+Q^2-1}\ \cot\left(\frac{\pi\left(l+2n-1\right)}{2\xi}\right) \quad \text{with} \quad n \in \mathbb{N}. \quad (4.57) $$

In these resonance conditions $\xi \ll l$, $\pi\left(l+2n\right) \gg 1$ and $\pi\left(l+2n-1\right) \gg 1$.

In Table 4.10 we present the resonance spectra of the super-extremal Kerr-Newman-type ECO in the near-critical regime for $b = 10^{-2}$, $l = m = 1$ and $Q = 0.5$. Here we compare the exact dimensionless surface radius, evaluating (4.41) and (4.42) for the variable z, with the approximated dimensionless surface radius, given by (4.56) and (4.57), respectively. Also the relative error was obtained, see (4.18).

		$z_c\left(n=1\right)$	$z_c\left(n=2\right)$	$z_c\left(z=3\right)$	$z_c\left(n=4\right)$	$z_c\left(n=5\right)$
Dirichlet	A	1.837×10^{-1}	1.100×10^{-1}	7.845×10^{-2}	6.085×10^{-2}	4.962×10^{-2}
	N	1.926×10^{-1}	1.119×10^{-1}	7.911×10^{-2}	6.116×10^{-2}	4.979×10^{-2}
	$E\left(\%\right)$	4.650	1.642	8.350×10^{-1}	5.054×10^{-1}	3.390×10^{-1}
Neumann	A	2.756×10^{-1}	1.377×10^{-1}	9.162×10^{-2}	6.856×10^{-2}	5.468×10^{-2}
	N	3.156×10^{-1}	1.414×10^{-1}	9.269×10^{-2}	6.900×10^{-2}	5.491×10^{-2}
	$E\left(\%\right)$	14.51	2.724	1.164	6.476×10^{-1}	4.131×10^{-1}

Table 4.10: Near-critical super-extremal Kerr-Newman-type ECOs with reflective Dirichlet or Neumann boundary conditions. Here we compare the approximated radius z_c (analytical - A) with the exact radius solution (numerical - N) of the super-extremal Kerr-Newman-type ECO by calculating the relative error, E (in %). Here we set $b = 10^{-2}$, $Q = 0.5$ and $l = m = 1$.

From Table 4.10 we observe that the dimensionless surface radius z_c decreases when we increase n, as expected. Also when we increase n we have a better agreement between the numerical and analytical dimensionless surface radius z_c. This can be observed by the relative error, where for both reflective boundary conditions it decreases when we increase n.

In a final remark, let us observe (4.56) and (4.57) when the cotangent argument is much smaller than unity. Here we can obtain the same approximation (4.37) and (4.38) for extremal case in the small x regime. So the super-extremal Kerr-Newman-type ECO when $a^2 + Q^2 \to 1$ starts to behave like the extremal case that we obtained in the last section.

Chapter 5

Charged massless scalar field on a Kerr-Newman-type ECO

In this chapter we shall generalize the results of Chapter 4 for horizonless Kerr-Newman-type ECOs with reflective surfaces linearly coupled to massless and charged scalar fields. Here we assume the same setup as in Chapter 4. However, due to the presence of a charged scalar field, the Klein-Gordon equation is now given by (2.13) for $\mu = 0$. Then the radial equation will have, in comparison with the uncharged case, extra terms due to scalar field charge q.

Here we also present the existence of discrete set of critical surface radii, $\{r_c\,(a, Q, q; n)_{n=1}^{n=\infty}\}$, in Kerr-Newman-type ECOs with reflective boundary conditions in three different regimes: sub-extremal regime $M > \sqrt{a^2+Q^2}$, extremal regime $M = \sqrt{a^2+Q^2}$, and the super-extremal regime $M < \sqrt{a^2+Q^2}$. These ECOs can also support spatially regular static (marginally-stable) charged scalar field configurations. For convenience we also set $M = 1$.

5.1 Sub-extremal Kerr-Newman

Let us start with the sub-extremal regime, $M > \sqrt{a^2+Q^2}$. To obtain the discrete sets of critical surface radii that marks the onset of superradiant instabilities in the Kerr-Newman spacetime, there is a unique family of static resonances that are characterized by the property (4.4). Imposing this property into (2.19), we obtain the ordinary differential equation

$$\Delta \frac{d}{dr}\left(\Delta \frac{dR\,(r)}{dr}\right) + \left[(am + qQr)^2 - \Delta\; l\,(l+1)\right] R\,(r) = 0. \tag{5.1}$$

This equation also has as solutions the hypergeometric function, ${}_2F_1\,(a, b; c; z)$. To obtain the standard form (Eq. 15.5.1 in [32]) from (5.1), we redefine the variable $R\,(r)$ as well as the independent variable r with the following expression:

$$R\,(x) = x^{-i\frac{\eta+qQ}{\tau}}\,(1-x)^{\frac{1+\delta}{2}}\,H\,(x)\,, \tag{5.2}$$

where

$$\tau \equiv \frac{r_+ - r_-}{r_+}, \quad \eta \equiv \frac{am}{r_+}, \quad \delta = \sqrt{(2l+1)^2 - 4q^2Q^2} \tag{5.3}$$

and x is given by (4.7). Here we recall that the variable x set the would-be horizon at the origin whereas the exterior spacetime is characterized by the interval of $0 < x \leq 1$. Moreover this change of variables is only valid for the non-extremal regime.

Applying these changes into (5.1) we obtain the following differential equation

$$\begin{aligned} x\left(1-x\right)\frac{d^{2}H\left(x\right)}{dx^{2}}+\left[\left(1-2i\frac{\eta+qQ}{\tau}\right)-\left(1+\delta-2i\frac{\eta+qQ}{\tau}+1\right)x\right]\frac{dH\left(x\right)}{dx} \\ +\left[i\frac{\eta+qQ}{\tau}\left(1+\delta\right)-\frac{1+\delta}{2}-l\left(l+1\right)+\frac{2\eta qQ}{\tau}+\frac{2q^{2}Q^{2}}{\tau}\right]H\left(x\right)=0, \end{aligned} \tag{5.4}$$

In terms of $R\left(x\right)$, the solution of (5.4) takes the form

$$\begin{aligned} R\left(x\right)=x^{-i\frac{\eta+qQ}{\tau}}\left(1-x\right)^{\frac{1+\delta}{2}}\left[A\ {}_{2}F_{1}\left(\frac{1}{2}\left[1+\delta-2iqQ\right],\frac{1}{2}\left[1+\delta-4i\frac{\eta+qQ}{\tau}+2iqQ\right];1+\delta;1-x\right)\right. \\ \left.+B\left(1-x\right)^{-\delta}\ {}_{2}F_{1}\left(\frac{1}{2}\left[1-2iqQ-\delta\right],\frac{1}{2}\left[1-\delta-4i\frac{\eta+qQ}{\tau}+2iqQ\right];1-\delta;1-x\right)\right]. \end{aligned} \tag{5.5}$$

where A and B are normalization constants.

Now let us impose the boundary condition (4.3). As we have seen, for $r\rightarrow\infty$ $(x\rightarrow1)$, the hypergeometric function behaves as ${}_{2}F_{1}\left(a,b;c;\left(1-x\right)\rightarrow0\right)\rightarrow1$. So from (5.5) we observe that the only term that obeys the boundary condition (4.3) is the first term. Thus $B=0$. Then the static resonances of the Kerr-Newman-type ECO are characterized by the radial function

$$R\left(x\right)=Ax^{-i\frac{\eta+qQ}{\tau}}\left(1-x\right)^{\frac{1+\delta}{2}}\ {}_{2}F_{1}\left(\tfrac{1}{2}\left[1+\delta-2iqQ\right],\tfrac{1}{2}\left[1+\delta-4i\tfrac{\eta+qQ}{\tau}+2iqQ\right];1+\delta;1-x\right). \tag{5.6}$$

At last, when applying (5.6) into the reflective boundary conditions (4.2), we can obtain the following compact resonance equations:

$${}_{2}F_{1}\left(\frac{1}{2}\left[1+\delta-2iqQ\right],\frac{1}{2}\left[1+\delta-4i\frac{\eta+qQ}{\tau}+2iqQ\right];1+\delta;1-x_{c}\right)=0, \tag{5.7}$$

for a Dirichlet boundary condition and

$$\begin{aligned} \frac{d}{dx}\left[x^{-i\frac{\eta+qQ}{\tau}}\left(1-x\right)^{\frac{1+\delta}{2}}\right. \\ \left.{}_{2}F_{1}\left(\frac{1}{2}\left[1+\delta-2iqQ\right],\frac{1}{2}\left[1+\delta-4i\frac{\eta+qQ}{\tau}+2iqQ\right];1+\delta;1-x\right)\right]_{x=x_{c}}=0, \end{aligned} \tag{5.8}$$

for a Neumann boundary conditions.

If we set $q=0$ we recover the same equations for the sub-extremal regime in Chapter 4. Thus these equations are a generalization of horizonless Kerr-Newman-type ECOs that supports static (marginally-stable) scalar field configurations.

5.1.1 Resonance spectra

Now let us proceed to the construction of the resonance spectra of (5.7) and (5.8) that we solve numerically. For the given physical parameters $\{a,Q,q,l,m\}$, we obtain a discrete set of critical radii, which can support spatially regular static scalar field resonances. Also, by fixing these physical parameters, we can study the (in)stabilities of the Kerr-Newman-type ECOs, where for $r_{c}<r_{c}^{\max}$ the Kerr-Newman-type ECO suffers from superradiant instabilities whereas for $r_{c}>r_{c}^{\max}$ the Kerr-Newman-type ECO is stable.

In this case, due to the extra term of the scalar field charge q, the resonance solutions will be different if we change this parameter, as we can observe from Fig.5.1.

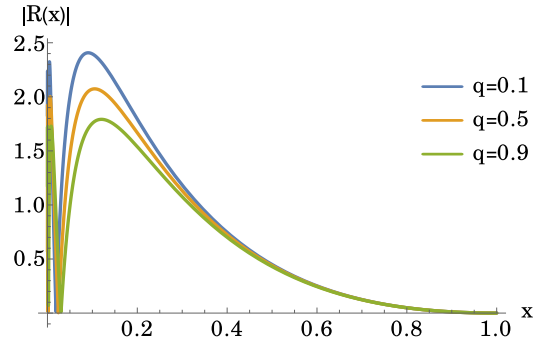

Figure 5.1: Radial profile of the sub-extremal Kerr-Newman-type ECO. Here we set $a = 0.9$, $Q = 0.3$ and $l = m = 1$ and change the scalar field charge q.

In Tables 5.1 we display the outermost dimensionless critical surface radius $z_c^{\max}(a, Q, q, l, m)$ of the Kerr-Newman-type ECO that can support static massless and charged scalar field configuration with reflective either Dirichlet or Neumann boundary conditions.

Dirichlet		$z_c^{\max}(a = 0.3)$	$z_c^{\max}(a = 0.5)$	$z_c^{\max}(a = 0.7)$	$z_c^{\max}(a = 0.9)$
$Q = 0.1$	$q = 0.1$	1.118×10^{-9}	4.562×10^{-6}	3.554×10^{-4}	1.168×10^{-2}
	$q = 0.5$	4.528×10^{-8}	1.790×10^{-5}	6.535×10^{-4}	1.485×10^{-2}
	$q = 0.9$	5.564×10^{-7}	5.269×10^{-5}	1.103×10^{-3}	1.850×10^{-2}
$Q = 0.5$	$q = 0.1$	2.964×10^{-7}	8.000×10^{-5}	3.051×10^{-3}	
	$q = 0.5$	2.221×10^{-4}	1.894×10^{-3}	1.402×10^{-2}	
	$q = 0.9$	2.934×10^{-3}	9.965×10^{-3}	3.778×10^{-2}	
$Q = 0.9$	$q = 0.1$	1.077×10^{-3}			
	$q = 0.5$	3.065×10^{-2}			
	$q = 0.9$	1.282×10^{-1}			

Neumann		$z_c^{\max}(a = 0.3)$	$z_c^{\max}(a = 0.5)$	$z_c^{\max}(a = 0.7)$	$z_c^{\max}(a = 0.9)$
$Q = 0.1$	$q = 0.1$	1.259×10^{-5}	8.517×10^{-4}	8.434×10^{-3}	5.942×10^{-2}
	$q = 0.5$	8.208×10^{-5}	1.755×10^{-3}	1.198×10^{-2}	6.992×10^{-2}
	$q = 0.9$	2.965×10^{-4}	3.141×10^{-3}	1.628×10^{-2}	8.136×10^{-2}
$Q = 0.5$	$q = 0.1$	2.054×10^{-4}	3.724×10^{-3}	2.716×10^{-2}	
	$q = 0.5$	6.968×10^{-3}	2.297×10^{-2}	7.294×10^{-2}	
	$q = 0.9$	3.202×10^{-2}	6.582×10^{-2}	1.468×10^{-1}	
$Q = 0.9$	$q = 0.1$	1.280×10^{-2}			
	$q = 0.5$	1.143×10^{-1}			
	$q = 0.9$	3.526×10^{-1}			

Table 5.1: Marginally-stable Kerr-Newman-type ECOs with reflective Dirichlet or Neumann boundary conditions. For different a, Q and q, we present the largest dimensionless radius $z_c^{\max}$ of the horizonless ECO that can support the spatially regular static charged scalar field configurations for $l = m = 1$.

Analysing the results obtained in Table 5.1, for both boundary conditions, we observe an increasing on the dimensionless critical surface radius $z_c^{\max}$ when raising the ECO spin a as well as the ECO charge Q, similarly to the sub-extremal regime in Chapter 4.

However, our main objective in this case is to study the behavior of the dimensionless critical surface radius $z_c^{\max}$ in the presence of a charged scalar field. By fixing the charge Q, when we increase the scalar field charge q, the dimensionless critical surface radius $z_c^{\max}$ increases. Also we observe an increase on $z_c^{\max}$ when we increase the angular momentum if we fix the two charges.

Now let us study the behavior of $z_c^{\max}$ for various equatorial modes $l = m$. In Table 5.2 we exhibit the largest dimensionless critical surface radius $z_c^{\max}$ of the horizonless Kerr-Newman-type ECO with

reflective Dirichlet or Neumann boundary conditions for various equatorial ($l = m$) scalar field modes. For a fixed $a = 0.5$, we have an increase in the dimensionless critical surface radius $z_c^{\max}$ when we increase the scalar field modes $l = m$. Also $z_c^{\max}$ increases when we increase the ECO charge Q or the scalar field charge q.

Dirichlet		$z_c^{\max}(l=1)$	$z_c^{\max}(l=2)$	$z_c^{\max}(l=3)$	$z_c^{\max}(l=4)$	$z_c^{\max}(l=5)$
$Q=0.1$	$q=0.1$	4.562×10^{-6}	4.301×10^{-4}	1.951×10^{-3}	4.199×10^{-3}	6.711×10^{-3}
	$q=0.5$	1.790×10^{-5}	6.594×10^{-4}	2.446×10^{-3}	4.866×10^{-3}	7.472×10^{-3}
	$q=0.9$	5.269×10^{-5}	9.649×10^{-4}	3.018×10^{-3}	5.597×10^{-3}	8.284×10^{-3}
$Q=0.7$	$q=0.1$	8.105×10^{-4}	6.376×10^{-3}	1.407×10^{-2}	2.161×10^{-2}	2.842×10^{-2}
	$q=0.5$	1.243×10^{-2}	2.231×10^{-2}	3.080×10^{-2}	3.792×10^{-2}	4.392×10^{-2}
	$q=0.9$	5.101×10^{-2}	5.187×10^{-2}	5.575×10^{-2}	5.972×10^{-2}	6.335×10^{-2}

Neumann		$z_c^{\max}(l=1)$	$z_c^{\max}(l=2)$	$z_c^{\max}(l=3)$	$z_c^{\max}(l=4)$	$z_c^{\max}(l=5)$
$Q=0.1$	$q=0.1$	8.517×10^{-4}	6.714×10^{-3}	1.340×10^{-2}	1.909×10^{-2}	2.376×10^{-2}
	$q=0.5$	1.755×10^{-3}	8.670×10^{-3}	1.553×10^{-2}	2.116×10^{-2}	2.569×10^{-2}
	$q=0.9$	3.141×10^{-3}	1.093×10^{-2}	1.785×10^{-2}	2.334×10^{-2}	2.771×10^{-2}
$Q=0.7$	$q=0.1$	1.246×10^{-2}	3.209×10^{-2}	4.650×10^{-2}	5.699×10^{-2}	6.492×10^{-2}
	$q=0.5$	6.886×10^{-2}	7.751×10^{-2}	8.384×10^{-2}	8.860×10^{-2}	9.231×10^{-2}
	$q=0.9$	1.883×10^{-1}	1.468×10^{-1}	1.339×10^{-1}	1.281×10^{-1}	1.251×10^{-1}

Table 5.2: Marginally-stable Kerr-Newman-type ECO with reflective Dirichlet or Neumann boundary conditions. For different $l = m$, Q and q, we present the largest dimensionless radius $z_c^{\max}$ of the horizonless ECO that can support the spatially regular static charged scalar field configurations for $a = 0.5$.

The only oddity from this results is when we have $Q = 0.7$ and $q = 0.9$ for the Neumann boundary condition. For these specific values, $z_c^{\max}$ decreases slightly when increasing the equatorial modes $l = m$.

5.1.2 Resonance spectra in the highly compact approximation

The resonances conditions (5.7) and (5.8) can also be solved analytically in the small x regime ($x \ll 1$), which corresponds to the family of highly compact Kerr-Newman-type ECOs. Following closely the same process done in Chapter 4, the radial equation (5.6) in the small x regime will be

$$\begin{aligned} R(x) =& A\Gamma(1+\delta)(1-x)^{\frac{1+\delta}{2}}\left[x^{-i\frac{\eta+qQ}{\tau}}\frac{\Gamma\left(-2i\frac{\eta+qQ}{\tau}\right)}{\Gamma\left(\frac{1}{2}\left[1+\delta+2iqQ-4i\frac{\eta+qQ}{\tau}\right]\right)\Gamma\left(\frac{1}{2}\left[1+\delta-2iqQ\right]\right)}\right. \\ &\left.+x^{i\frac{\eta+qQ}{\tau}}\frac{\Gamma\left(-2i\frac{\eta+qQ}{\tau}\right)}{\Gamma\left(\frac{1}{2}\left[1+\delta+2iqQ-4i\frac{\eta+qQ}{\tau}\right]\right)\Gamma\left(\frac{1}{2}\left[1+\delta-2iqQ\right]\right)}\right]. \end{aligned} \tag{5.9}$$

Now we can apply the small-x spatial behavior (5.9) into the boundary conditions (5.7) and (5.8). From the approximation we obtain two discrete sets $\{x_c^{\mathrm{D}}(a,Q,q,l,m)_{n=1}^{n=\infty}\}$ and $\{x_c^{\mathrm{N}}(a,Q,q,l,m)_{n=1}^{n=\infty}\}$, each one labelled by an integer number n, in a compact analytical formula, which take the form

$$x_c^{\mathrm{D}}(n) = e^{-\frac{\pi\left(n+\frac{1}{2}\right)}{\gamma}}\left[\frac{\Gamma(2i\gamma)\Gamma\left(\frac{1}{2}\left[1+\delta-4i\gamma+2iqQ\right]\right)\Gamma\left(\frac{1}{2}\left[1+\delta-2iqQ\right]\right)}{\Gamma(-2i\gamma)\Gamma\left(\frac{1}{2}\left[1+\delta+4i\gamma-2iqQ\right]\right)\Gamma\left(\frac{1}{2}\left[1+\delta+2iqQ\right]\right)}\right]^{\frac{1}{2i\gamma}}, \quad n\in\mathbb{N}, \tag{5.10}$$

and

$$x_c^{\mathrm{N}}(n) = e^{-\frac{\pi n}{\gamma}}\left[\frac{\Gamma(2i\gamma)\Gamma\left(\frac{1}{2}\left[1+\delta-4i\gamma+2iqQ\right]\right)\Gamma\left(\frac{1}{2}\left[1+\delta-2iqQ\right]\right)}{\Gamma(-2i\gamma)\Gamma\left(\frac{1}{2}\left[1+\delta+4i\gamma-2iqQ\right]\right)\Gamma\left(\frac{1}{2}\left[1+\delta+2iqQ\right]\right)}\right]^{\frac{1}{2i\gamma}}, \quad n\in\mathbb{N}, \tag{5.11}$$

where $\gamma = \frac{\eta + qQ}{\tau}$ for simplification.

With these discrete sets of the dimensionless critical radii we can compare with the resonance spectra derived in (5.7) and (5.8). In Table 5.3 we present the values for the dimensionless radius z_c of the Kerr-Newman-type ECO with reflecting Dirichlet or Neumann boundary conditions, where we compare the results obtained analytically through the compact equations (5.10) and (5.11) with the results obtained numerically through the equations (5.7) and (5.8). In these tables we fix the angular momentum $a = 0.9$, the scalar field mode $l = m = 1$ and the charge $Q = 0.3$, changing the scalar field charge q. The relative error is also displayed.

Dirichlet		$z_c\,(n=1)$	$z_c\,(n=2)$	$z_c\,(n=3)$	$z_c\,(n=4)$
$q=0.1$	A	2.688×10^{-2}	3.091×10^{-3}	3.708×10^{-4}	4.470×10^{-5}
	N	2.751×10^{-2}	3.099×10^{-3}	3.709×10^{-4}	4.471×10^{-5}
	$E\,(\%)$	2.300	2.518×10^{-1}	3.004×10^{-2}	3.619×10^{-3}
$q=0.5$	A	4.429×10^{-2}	6.726×10^{-3}	1.088×10^{-3}	1.775×10^{-4}
	N	4.534×10^{-2}	6.748×10^{-3}	1.088×10^{-3}	1.776×10^{-4}
	$E\,(\%)$	2.304	3.224×10^{-1}	5.147×10^{-2}	8.385×10^{-3}
$q=0.9$	A	6.714×10^{-2}	1.241×10^{-2}	2.499×10^{-3}	5.111×10^{-4}
	N	6.840×10^{-2}	1.245×10^{-2}	2.500×10^{-3}	5.112×10^{-4}
	$E\,(\%)$	1.848	2.963×10^{-1}	5.800×10^{-2}	1.180×10^{-2}

Neumann		$z_c\,(n=1)$	$z_c\,(n=2)$	$z_c\,(n=3)$	$z_c\,(n=4)$
$q=0.1$	A	8.647×10^{-2}	9.007×10^{-3}	1.069×10^{-3}	1.287×10^{-4}
	N	9.822×10^{-2}	9.091×10^{-3}	1.070×10^{-3}	1.287×10^{-4}
	$E\,(\%)$	11.95	9.225×10^{-1}	1.065×10^{-1}	1.279×10^{-2}
$q=0.5$	A	1.267×10^{-1}	1.698×10^{-2}	2.698×10^{-3}	4.392×10^{-4}
	N	1.421×10^{-1}	1.715×10^{-2}	2.702×10^{-3}	4.393×10^{-4}
	$E\,(\%)$	10.85	9.888×10^{-1}	1.499×10^{-1}	2.422×10^{-2}
$q=0.9$	A	1.782×10^{-1}	2.827×10^{-2}	5.548×10^{-3}	1.129×10^{-3}
	N	1.954×10^{-1}	2.850×10^{-2}	5.556×10^{-3}	1.130×10^{-3}
	$E\,(\%)$	8.839	8.172×10^{-1}	1.472×10^{-1}	2.946×10^{-2}

Table 5.3: Sub-extremal Kerr-Newman-type ECO with reflective Dirichlet or Neumann Neumann boundary condition. Here we compare the approximated radius z_c (analytical - A) with the exact radius solution (numerical - N) of the horizonless sub-extremal Kerr-Newman-type ECO by calculating the relative error, E (in %). The values were obtained for $a = 0.9$, $Q = 0.3$ and $l = m = 1$ where we change the value for the scalar field charge q.

We can see in Table 5.3, specially for $z_c \ll 1$, a good agreement between the approximated radius of the ECO and the exact radius solution for every scalar field charge value. We also observe that the relative error (4.18) decreases as we increase the value of n.

For $Q = 0$ and $q = 0$, in all the data obtained, we have a good match with the results presented in [1].

5.2 Extremal Kerr-Newman

We now tackle the extremal case. In this case, the radial equation, by imposing the property (4.4) will be (5.1) where we now consider the extremal condition $M = \sqrt{a^2 + Q^2}$. To solve (5.1), for the extremal case, we redefine the dependent and independent variable through (4.20) and (4.21), respectively, as we have done in Chapter 4. Performing these transformations into the radial equation, (5.1) we obtain

$$z^2 \frac{d^2 W(z)}{dz^2} + \left\{ \frac{[am + qQ(z+1)]^2}{z^2} - l(l+1) \right\} W(z) = 0. \tag{5.12}$$

By solving (5.12) in MATHEMATICA 11 it was not possible to obtain solutions. So, in order to properly solve (5.12) we change again the independent variable z to

$$y = \frac{am + qQ}{z} = \frac{\kappa}{z}. \tag{5.13}$$

Changing to this new variable, the radial equation (5.12) takes the form

$$y^2 \frac{d^2W(y)}{dy^2} + 2y\frac{dW(y)}{dy} + \left\{ (y + qQ)^2 - l(l+1) \right\} W(y) = 0, \tag{5.14}$$

which solutions, in terms of $R(z)$, will be

$$\begin{aligned} R(z) = e^{-\frac{i\kappa}{z}} \kappa^{-\frac{1-\delta}{2}} z^{-\frac{1+\delta}{2}} \Bigg[& CU\left(\frac{1}{2}\left[1 + 2iqQ + \delta\right], 1+\delta, \frac{2i\kappa}{z}\right) \\ & + D\frac{\Gamma\left(\frac{1}{2} - iqQ + \frac{\delta}{2}\right)}{\Gamma(\delta+1)\Gamma\left(\frac{1}{2} - iqQ - \frac{\delta}{2}\right)} M\left(\frac{1}{2}\left[1 + 2iqQ + \delta\right], 1+\delta, \frac{2i\kappa}{z}\right)\Bigg], \end{aligned} \tag{5.15}$$

where C and D are normalization constants and $\delta > 0$ is given by (5.3).

Now let us impose the boundary condition (4.3). So for $r \to \infty$, the new variable will also behave as $z \to \infty$. Then the radial equation (5.15) near spatial infinity approximates to

$$R(z) \overset{z\to\infty}{=} \kappa^{-\frac{1-\delta}{2}} z^{-\frac{1+\delta}{2}} \left[C\frac{\Gamma(1+\delta)}{\Gamma\left(\frac{1}{2} + iqQ + \frac{\delta}{2}\right)} (2i\kappa)^{-\delta} z^{\delta} + D\frac{\Gamma\left(\frac{1}{2} - iqQ + \frac{\delta}{2}\right)}{\Gamma(\delta+1)\Gamma\left(\frac{1}{2} - iqQ - \frac{\delta}{2}\right)} \right]. \tag{5.16}$$

To obey the asymptotic behavior (4.3) we require that the normalization constant C is zero. Note that the second term is a constant, however the term $z^{-(1+\delta)/2}$ is the determinant factor to satisfy (4.3). Then the radial solution is now

$$R(z) = De^{-\frac{i\kappa}{z}} \kappa^{-\frac{1-\delta}{2}} z^{-\frac{1+\delta}{2}} \frac{\Gamma\left(\frac{1}{2} - iqQ + \frac{\delta}{2}\right)}{\Gamma(\delta+1)\Gamma\left(\frac{1}{2} - iqQ - \frac{\delta}{2}\right)} M\left(\frac{1}{2}\left[1 + 2iqQ + \delta\right], 1+\delta, \frac{2i\kappa}{z}\right). \tag{5.17}$$

By plotting the radial solution (5.17) we can clearly see the infinite resonance conditions (see Fig 5.2).

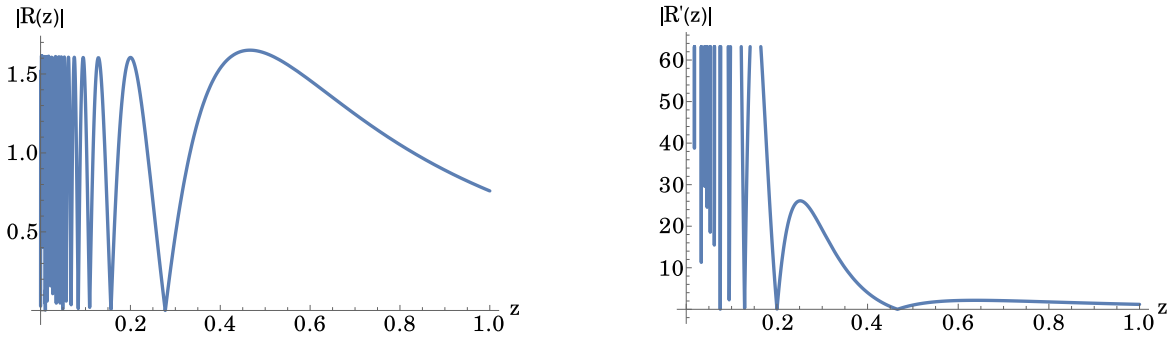

Figure 5.2: Radial profile of the extremal Kerr-Newman-type ECO (left panel) and its derivative (right panel). These plots were obtained for $Q = 0.5$, $l = m = 1$ and $q = 0.5$.

At last we impose the reflective boundary condition (4.2), and we obtain a set of resonance equations for each boundary condition that will be given as

$$\begin{cases} e^{-\frac{i\kappa}{z_c}} z_c^{-\frac{1+\delta}{2}} M\left(\frac{1}{2}\left[1 + 2iqQ + \delta\right], 1+\delta, \frac{2i\kappa}{z_c}\right) = 0 & , \quad \text{for Dirichlet,} \\ \frac{d}{dz}\left[e^{-\frac{i\kappa}{z}} z^{-\frac{1+\delta}{2}} M\left(\frac{1}{2}\left[1 + 2iqQ + \delta\right], 1+\delta, \frac{2i\kappa}{z}\right)\right]\Big|_{z=z_c} = 0 & , \quad \text{for Neumann.} \end{cases} \tag{5.18}$$

5.2.1 Resonance spectra

With the resonance equations obtained in (5.18) we can now construct the discrete set of surface radii, $\{r_c\,(a,Q,q,m;n)_{n=1}^{n=\infty}\}$ for each reflective boundary condition in which the Kerr-Newman-type ECO supports static (marginally-stable) charged scalar field configurations. In here we will determine the outermost dimensionless critical radius that marks the boundary between stable and unstable extremal Kerr-Newman-type ECOs.

Another thing that we will study is the transition between the results obtained from (5.7) and (5.8) with the results obtained from (5.18). Here we try to approximate $a^2+Q^2\to 1$ in (5.7) and (5.8) and see if it converges to the set (5.18) (see Fig. 5.3)

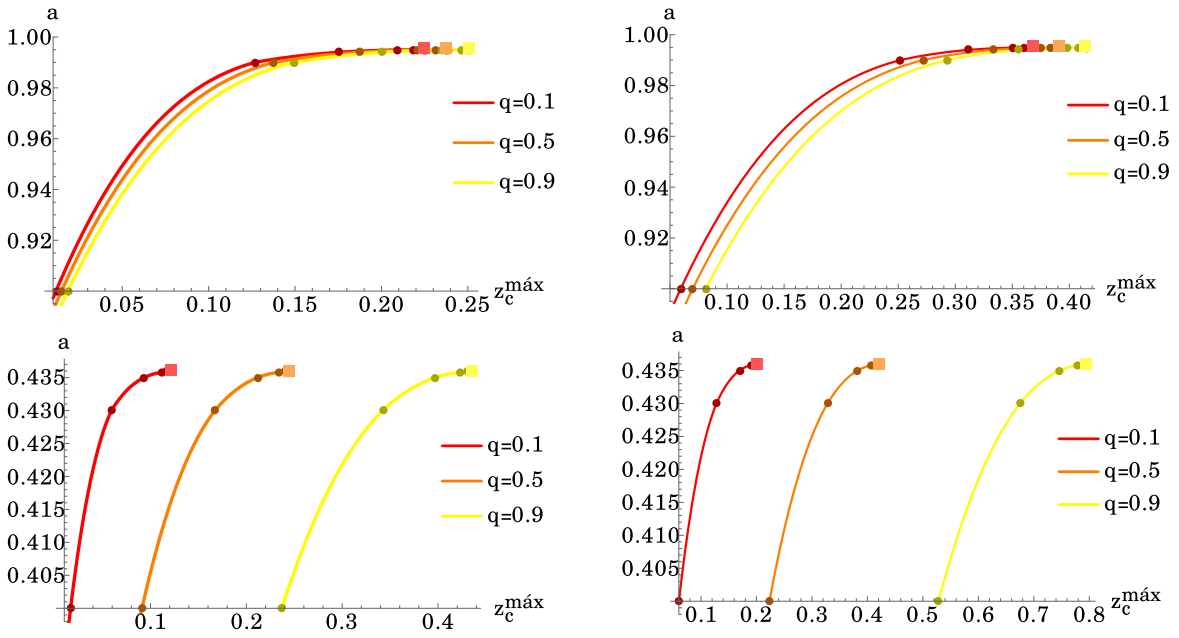

Figure 5.3: Convergence of the largest dimensionless critical surface radius $z_c^{\max}$, that corresponds to the transition between the results obtained in (5.7) and (5.8) when $a\to\sqrt{1-Q^2}$ and (5.18) when $a=\sqrt{1-Q^2}$ for the Dirichlet resonance condition (the two plots in the left panel) and Neumann resonance condition (the two plots in the right panel). The data (dots) obtained by the resonance conditions of (5.7) and (5.8) clearly converges to the values obtained by (5.18) (square). The values were obtained for $l=m=1$, for two different values of Q ($Q=0.1$ and $Q=0.9$) and three different values of q ($q=0.1$, $q=0.5$ and $q=0.9$).

We observe, from Fig. 5.3, that for $a^2+Q^2\to 1$, for the two different values of Q and the three values of q, the $z_c^{\max}$ obtained by the resonance conditions (5.7) and (5.8) will tend to $z_c^{\max}$ obtained by the resonance conditions (5.18). Also we observe that for a specific charge Q, $z_c^{\max}$ increases when we increase the scalar field charge q. Then we can conclude that the hypergeometric function for $a^2+Q^2\to 1$ will behave like the confluent hypergeometric function of the first kind.

Now let us study for a fixed charge Q - which consequently means a fixed angular momentum a - by changing the harmonic indices $\{l,m\}$ and the scalar field charge q. In Table 5.4 we display various values of the $z_c^{\max}$ by changing the scalar field modes $l=m$ and the scalar field charge q. Here we fix the ECO charge to $Q=0.9$.

		$z_c^{\max}\,(l=1)$	$z_c^{\max}\,(l=2)$	$z_c^{\max}\,(l=3)$	$z_c^{\max}\,(l=4)$	$z_c^{\max}\,(l=5)$
Dirichlet	$q=0.1$	1.216×10^{-1}	1.713×10^{-1}	2.040×10^{-1}	2.277×10^{-1}	2.459×10^{-1}
	$q=0.5$	2.443×10^{-1}	2.636×10^{-1}	2.791×10^{-1}	2.913×10^{-1}	3.013×10^{-1}
	$q=0.9$	4.355×10^{-1}	3.829×10^{-1}	3.693×10^{-1}	3.648×10^{-1}	3.637×10^{-1}
Neumann	$q=0.1$	2.008×10^{-1}	2.561×10^{-1}	2.874×10^{-1}	3.079×10^{-1}	3.226×10^{-1}
	$q=0.5$	4.203×10^{-1}	4.019×10^{-1}	3.978×10^{-1}	3.972×10^{-1}	3.977×10^{-1}
	$q=0.9$	7.953×10^{-1}	5.979×10^{-1}	5.336×10^{-1}	5.018×10^{-1}	4.831×10^{-1}

Table 5.4: Marginally-stable extremal Kerr-Newman-type ECO with reflective Dirichlet or Neumann boundary condition. Here we present $z_c^{\max}$ of the horizonless extremal Kerr-Newman-type ECO for different equatorial modes, $l=m$, and scalar field charge q by fixing $Q=0.9$.

Observing Table 5.4, for a fixed q we can see different behaviors at $z_c^{\max}$. For $q=0.1$ we observe an increase of $z_c^{\max}$ when we increase the equatorial modes for both reflective boundary conditions, which is the typical behavior. If we set $q=0.5$ we observe the typical increase of $z_c^{\max}$ for the Dirichlet boundary condition, however for the Neumann boundary condition, $z_c^{\max}$ decreases by increasing the equatorial modes. Also we observe this decreasing in $z_c^{\max}$ for $q=0.9$ in both boundary conditions. This looks like the largest surface radius has a maximum value even if we increase the equatorial modes.

By fixing $l=m$ we observe an increase of $z_c^{\max}$ when we increase q for both boundary conditions.

5.2.2 Resonance spectra in the highly compact approximation

Now let us perform an approximation for the small regime $z\ll1$ in the resonance conditions (5.18) that corresponds to the family of highly compact extremal Kerr-Newman-type ECOs. Considering this regime, we can obtain a simple form for the radial equation (5.17), given by the following expression:

$$R\left(z\right)\overset{z\to0}{=}C\,\kappa^{-1}\frac{2^{\frac{1-\delta}{2}}e^{-\frac{\pi qQ}{2}}\Gamma\left(\frac{1}{2}-iqQ+\frac{\delta}{2}\right)}{\Gamma\left(\frac{1}{2}-iqQ-\frac{\delta}{2}\right)\left|\Gamma\left(\frac{1}{2}+\frac{\delta}{2}+iqQ\right)\right|}\sin\left(\frac{\kappa}{z}+qQ\ln\left(\frac{2\kappa}{z}\right)-\mathbf{arg}\Gamma\left(\frac{1}{2}+iqQ+\frac{\delta}{2}\right)-\frac{\pi\delta}{4}+\frac{\pi}{4}\right).\tag{5.19}$$

Imposing the reflective boundary conditions (4.2) into the approximation (5.19) we obtain two discrete sets for $\{z_c^{\rm D}\left(a,Q,q,l,m;n\right)_{n=1}^{n=\infty}\}$ and for $\{z_c^{\rm N}\left(a,Q,q,l,m;n\right)_{n=1}^{n=\infty}\}$, where the compact formulas are given by

$$z_c^{\rm D}\left(n\right)=\frac{\kappa}{qQ\,\mathbf{ProductLog}\left[\frac{e^{\frac{\pi}{4qQ}\left(4n+\delta-1\right)+\frac{\mathbf{arg}\Gamma\left(\frac{1}{2}+\frac{\delta}{2}+iqQ\right)}{qQ}}}{2qQ}\right]}\quad n\in\mathbb{N},\tag{5.20}$$

and

$$z_c^{\rm N}\left(n\right)=\frac{\kappa}{qQ\,\mathbf{ProductLog}\left[\frac{e^{\frac{\pi}{4qQ}\left(4n+\delta-3\right)+\frac{\mathbf{arg}\Gamma\left(\frac{1}{2}+\frac{\delta}{2}+iqQ\right)}{qQ}}}{2qQ}\right]}\quad n\in\mathbb{N}\,,\tag{5.21}$$

respectively. Here **ProductLog** is a routine in MATHEMATICA 11 which corresponds to the inverse of $f\left(x\right)=xe^{x}$ in the principal branch. This is also denominated as the Lambert W function.

In Table 5.5 we display the dimensionless critical surface radius z_c of the analytical compact formulas (5.20) and (5.21), and the numerically resonance equation (5.18). There we compare the results obtained analytically and numerically through the relative error, given by (4.18), for the equatorial mode $l=m=1$ and $Q=0.1$ by changing the scalar field charge q.

Dirichlet		$z_c\,(n=1)$	$z_c\,(n=2)$	$z_c\,(n=3)$	$z_c\,(n=4)$	$z_c\,(n=5)$
$q=0.1$	A	2.141×10^{-1}	1.283×10^{-1}	9.162×10^{-2}	7.124×10^{-2}	5.827×10^{-2}
	N	2.246×10^{-1}	1.305×10^{-1}	9.239×10^{-2}	7.160×10^{-2}	5.847×10^{-2}
	$E\,(\%)$	4.900	1.674	8.419×10^{-1}	5.062×10^{-1}	3.378×10^{-1}
$q=0.5$	A	2.261×10^{-1}	1.351×10^{-1}	9.621×10^{-2}	7.469×10^{-2}	6.103×10^{-2}
	N	2.375×10^{-1}	1.374×10^{-1}	9.703×10^{-2}	7.508×10^{-2}	6.124×10^{-2}
	$E\,(\%)$	5.011	1.704	8.548×10^{-1}	5.130×10^{-1}	3.418×10^{-1}
$q=0.9$	A	2.386×10^{-1}	1.420×10^{-1}	1.009×10^{-1}	7.822×10^{-2}	6.384×10^{-2}
	N	2.508×10^{-1}	1.444×10^{-1}	1.018×10^{-1}	7.862×10^{-2}	6.406×10^{-2}
	$E\,(\%)$	5.127	1.736	8.683×10^{-1}	5.200×10^{-1}	3.459×10^{-1}

Neumann		$z_c\,(n=1)$	$z_c\,(n=2)$	$z_c\,(n=3)$	$z_c\,(n=4)$	$z_c\,(n=5)$
$q=0.1$	A	3.213×10^{-1}	1.605×10^{-1}	1.069×10^{-1}	8.015×10^{-2}	6.410×10^{-2}
	N	3.681×10^{-1}	1.649×10^{-1}	1.069×10^{-1}	8.067×10^{-2}	6.437×10^{-2}
	$(E\%)$	14.56	2.732	1.165	6.462×10^{-1}	4.109×10^{-1}
$q=0.5$	A	3.403×10^{-1}	1.692×10^{-1}	1.124×10^{-1}	8.410×10^{-2}	6.718×10^{-2}
	N	3.907×10^{-1}	1.739×10^{-1}	1.137×10^{-1}	8.465×10^{-2}	6.746×10^{-2}
	$E\,(\%)$	14.80	2.778	1.182	6.544×10^{-1}	4.155×10^{-1}
$q=0.9$	A	3.600×10^{-1}	1.781×10^{-1}	1.180×10^{-1}	8.813×10^{-2}	7.030×10^{-2}
	N	4.142×10^{-1}	1.831×10^{-1}	1.194×10^{-1}	8.871×10^{-2}	7.060×10^{-2}
	$E\,(\%)$	15.00	2.827	1.200	6.629×10^{-1}	3.459×10^{-1}

Table 5.5: Extremal Kerr-Newman-type ECO with reflective Dirichlet or Neumann boundary conditions. Here we compare the approximated dimensionless radius z_c (analytical - A) with the exact dimensionless radius solution (numerical - N) by calculating the relative error, E (in %). The values were obtained for $l=m=1$ and $Q=0.1$ by changing q.

From Table 5.5 we observe, for both boundary conditions, a good agreement between the approximated dimensionless radius obtained by (5.20) and (5.21) and the exact dimensionless radius solution obtained by (5.18). This is observed through the relative error which decreases when we increase the parameter n. Also this is valid for all values of q.

5.3 Super-extremal Kerr-Newman

Let us now consider the super-extremal case where $M<\sqrt{a^2+Q^2}$. Here we will obtain the finite discrete family set of critical surface radius $r_c\,(a,Q,q,l,m;n)_{n=1}^{n=N}$, as we have seen in Chapter 4, of the super-extremal Kerr-Newman-type ECO that can support (marginally-stable) charged scalar field configurations.

Imposing the property (4.4) into the radial equation (2.19) for $\mu=0$ we obtain the same radial differential equation (5.1) which solutions are given by the radial equation (5.5). However, due to the condition $M<\sqrt{a^2+Q^2}$ we will have an imaginary factor in the quantities $r_\pm$ ($r_\pm=M\pm i\sqrt{a^2+Q^2-M^2}$). Then the radial equation, in this case, already obeying the condition (4.3), is given by

$$R\,(x)=Ax^{-\frac{\sigma+iqQ}{2}}\,(1-x)^{\frac{1+\delta}{2}}\;\;{}_2F_1\left(\frac{1}{2}\left[1+\delta-2iqQ\right],\frac{1}{2}\left[1+\delta-2\sigma\right];1+\delta;1-x\right), \tag{5.22}$$

where A is a normalization constant, x is given by (4.7) and σ is

$$\sigma=\frac{am+qQ}{\sqrt{a^2+Q^2-M^2}}. \tag{5.23}$$

At last we impose the reflective boundary conditions and obtain the following compact resonance

conditions:

$$ {}_2F_1\left(\frac{1}{2}\left[1+\delta-2iqQ\right],\frac{1}{2}\left[1+\delta-2\sigma\right];1+\delta;1-x_c\right)=0, \tag{5.24}$$

for a Dirichlet boundary condition and

$$ \frac{d}{dx}\left[x^{-\frac{\sigma+iqQ}{2}}\left(1-x\right)^{\frac{1+\delta}{2}}\ {}_2F_1\left(\frac{1}{2}\left[1+\delta-2iqQ\right],\frac{1}{2}\left[1+\delta-2\sigma\right];1+\delta;1-x\right)\right]_{x=x_c}=0, \tag{5.25}$$

for a Neumann boundary condition.

Before presenting the resonance spectra there are some properties about the radial equation (5.22) that are important to discuss. As we have seen for the super-extremal Kerr-Newman-type ECO, in Chapter 4, the radial equation is symmetric for $r = M$. However, for this case, even after performing the variable change $x \to z$ (see (4.21)) we cannot visualize such property due to the scalar field charge q. In Fig.5.4 we observe that (5.22) is not symmetric for $z = 0$ (or $r = M$) and appears to have a discontinuity at this value although the limit when $z \to 0$, approaching from both function sides, tends to the same point.

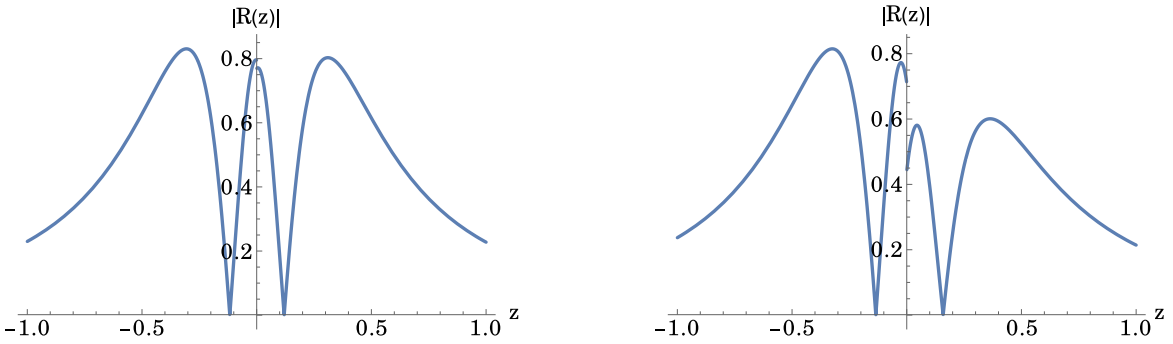

Figure 5.4: Radial profile of (5.22) in terms of z for $q = 0.1$ (left panel) and $q = 0.5$ (right panel). Here we set $Q = 0.1$, $l = m = 1$ and $a \sim 0.985$.

However if we derive (5.22) and perform the limit for the same value we will have an one-side limit. So in the following sections we will only consider the values of $z \in [0, 1]$.

Another property of (5.22) is the existence of finite solutions. This can be observed from the Fig. 5.5, however in this case we cannot predict the possible number of resonance solutions through an expression, as we have seen for the super-extremal Kerr-Newman-type ECO in Chapter 4.

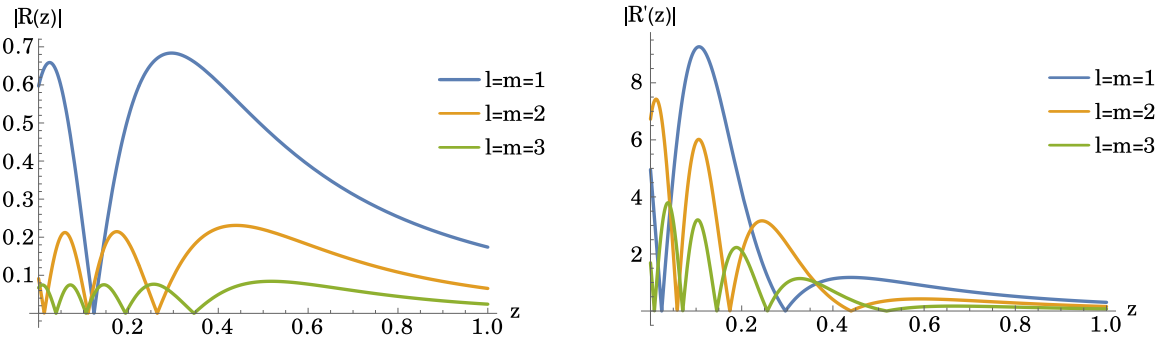

Figure 5.5: Radial profile of (5.22) in terms of z (left panel) and its derivative (right panel). Here we set $Q = 0.5$, $l = m = 1$, $q = 0.1$ and $a \sim 0.985$.

With these properties in mind we can construct more easily the resonance spectra of the super-extremal Kerr-Newman-type ECO that supports static (marginally-stable) charged scalar field configurations.

5.3.1 Regime of existence

To fully describe the composed super-extremal Kerr-Newman-type ECO it is necessary to determine the upper bound on the characteristic surface radius $\{r_c\,(a,Q,q,l,m;n)_{n=1}^{n=N}\}$ where this system exists. Let us introduce a new scalar function that is given by (4.46). Substituting into (5.1), we obtain a simple differential ordinary equation

$$\Delta^2\frac{d^2U\,(r)}{dr^2}+\left[(ma+qQr)^2-l\,(l+1)\,\Delta-\left(a^2+Q^2-1\right)\right]U\,(r)=0. \tag{5.26}$$

Due to the imposed boundary conditions (4.2) and (4.3) the scalar function $U\,(r)$ should have at least one extremum point $r=r_p$, in the interval $[r_c,\infty[$. So (4.46) obeys the relation (4.8). From these relations we can obtain an inequality which implies

$$\frac{qQam-l(l+1)}{l(l+1)-q^2Q^2}\,(1-\varpi)<r_p<\frac{qQam-l(l+1)}{l(l+1)-q^2Q^2}\,(1+\varpi)\,, \tag{5.27}$$

where

$$\varpi=\sqrt{1-\frac{\left\{a^2\left[1+l\,(l+1)-m^2\right]+Q^2\left[l\,(l+1)+1\right]-1\right\}\left[q^2Q^2-l\,(l+1)\right]}{\left[qQma+l\,(l+1)\right]^2}}. \tag{5.28}$$

By taking in consideration these relations and (4.21), for positive values of z, we can deduce that the super-extremal Kerr-Newman-type ECO is characterized by the upper bound

$$z_c<\frac{qQam-l(l+1)}{l(l+1)-q^2Q^2}\,(1+\varpi)-1. \tag{5.29}$$

In addition to this upper bound, we observe that $\varpi>0$ to obey (5.29). This means that the second term of ϖ obeys the inequality

$$\frac{\left\{a^2\left[1+l\,(l+1)-m^2\right]+Q^2\left[l\,(l+1)+1\right]-1\right\}\left[q^2Q^2-l\,(l+1)\right]}{\left[qQma+l\,(l+1)\right]^2}\leq 1. \tag{5.30}$$

Then we can calculate the possible range of values for the angular momentum a, that will be bounded by

$$\sqrt{1-Q^2}<a<\frac{l\,(l+1)\,mqQ+\sqrt{\chi\left[l\,(l+1)-q^2Q^2\right]\left[l\,(l+1)\,(\chi-m^2)\,(1-Q^2)+q^2Q^2\,(\chi Q^2-1)\right]}}{l\,(l+1)\,(\chi-m^2)-\chi q^2Q^2}, \tag{5.31}$$

where $\chi=l\,(l+1)+1$.

In Chapter 4 it was possible to determine a stronger upper bound for the angular momentum a for the super-extremal Kerr-Newman-type ECO that supports static massless scalar field configurations. However, here we could not established that stronger upper bound.

5.3.2 Resonance spectra

Now that we established the possible range of values for the dimensionless surface radius z_c we can construct the resonance spectrum for the Dirichlet boundary condition, $\{r_c\,(a,Q,q,l,m;n)_{n=1}^{n=N_d}\}$, and for the Neumann boundary condition, $\{r_c\,(a,Q,q,l,m;n)_{n=1}^{n=N_n}\}$, which characterizes the super-extremal Kerr-Newman-type ECO that supports static (marginally-stable) charged scalar field configurations. Due to the impossibility to construct a stronger upper bound for a, here we use the expression (4.54) where we choose $0<b\leq 0.3$ for convenience.

In Table 5.6, we present the largest dimensionless surface radius $z_c^{\max}$ for the Dirichlet and Neumann boundary conditions. Here we change the parameter b according to its range of values, the charge Q and q by fixing the equatorial modes at $l = m = 1$. The finite number of resonance solutions were not presented in this case.

Dirichlet		$z_c^{\max}$ $(b = 0.30)$	$z_c^{\max}$ $(b = 0.25)$	$z_c^{\max}$ $(b = 0.20)$	$z_c^{\max}$ $(b = 0.15)$
$Q = 0.1$	$q = 0.1$	6.080×10^{-2}	1.198×10^{-1}	1.615×10^{-1}	1.906×10^{-1}
	$q = 0.5$	8.499×10^{-2}	1.393×10^{-1}	1.781×10^{-1}	2.054×10^{-1}
	$q = 0.9$	1.084×10^{-1}	1.587×10^{-1}	1.949×10^{-1}	2.205×10^{-1}
$Q = 0.9$	$q = 0.1$	6.720×10^{-2}	8.602×10^{-2}	9.984×10^{-2}	1.098×10^{-1}
	$q = 0.5$	2.209×10^{-1}	2.286×10^{-1}	2.345×10^{-1}	2.389×10^{-1}
	$q = 0.9$	4.253×10^{-1}	4.287×10^{-1}	4.313×10^{-1}	4.332×10^{-1}

Neumann		$z_c^{\max}$ $(b = 0.30)$	$z_c^{\max}$ $(b = 0.25)$	$z_c^{\max}$ $(b = 0.20)$	$z_c^{\max}$ $(b = 0.15)$
$Q = 0.1$	$q = 0.1$	2.810×10^{-1}	3.104×10^{-1}	3.326×10^{-1}	3.487×10^{-1}
	$q = 0.5$	3.092×10^{-1}	3.367×10^{-1}	3.573×10^{-1}	3.724×10^{-1}
	$q = 0.9$	3.380×10^{-1}	3.636×10^{-1}	3.829×10^{-1}	3.971×10^{-1}
$Q = 0.9$	$q = 0.1$	1.718×10^{-1}	1.814×10^{-1}	1.888×10^{-1}	1.942×10^{-1}
	$q = 0.5$	4.105×10^{-1}	4.137×10^{-1}	4.162×10^{-1}	4.180×10^{-1}
	$q = 0.9$	7.962×10^{-1}	7.959×10^{-1}	7.957×10^{-1}	7.955×10^{-1}

Table 5.6: Marginally-stable super-extremal Kerr-Newman-type ECOs with reflective Dirichlet or Neumann boundary conditions. For different values of b, charge Q and scalar field charge q, we present $z_c^{\min}$ and $z_c^{\max}$ of the horizonless ECO that can support spatially regular static charged scalar field configurations $l = m = 1$.

From Table 5.6 we observe that for a fixed value of Q and q, the largest dimensionless surface radius $z_c^{\max}$, for both boundary conditions, increases as we decrease the parameter b (or as we decrease a). The only exception occurs when we set $Q = 0.9$ and $q = 0.9$ for the Neumann boundary condition, where $z_c^{\max}$ slightly decreases as we decrease b. This means, for this case, the surface radius that marks the onset of superradiant instabilities tends to increase when the angular momentum increases, differently from the other values. Although we do not present the number of resonance solutions, we can claim that increases when we decrease b.

If we fix Q and b, $z_c^{\max}$ increases with scalar field charge q, for both resonance conditions.

Now let us proceed to study the behavior of $z_c^{\max}$ for various equatorial modes $l = m$ displayed in Table 5.7. Here we fix the parameter $b = 0.25$ and $Q = 0.9$ by changing q.

		$z_c^{\max}$ $(l = 1)$	$z_c^{\max}$ $(l = 2)$	$z_c^{\max}$ $(l = 3)$	$z_c^{\max}$ $(l = 4)$	$z_c^{\max}$ $(l = 5)$
Dirichlet	$q = 0.1$	8.602×10^{-2}	1.488×10^{-1}	1.867×10^{-1}	2.133×10^{-1}	2.334×10^{-1}
	$q = 0.5$	2.286×10^{-1}	2.507×10^{-1}	2.680×10^{-1}	2.816×10^{-1}	2.925×10^{-1}
	$q = 0.9$	4.287×10^{-1}	3.759×10^{-1}	3.626×10^{-1}	3.586×10^{-1}	3.578×10^{-1}
Neumann	$q = 0.1$	1.814×10^{-1}	2.436×10^{-1}	2.778×10^{-1}	2.300×10^{-1}	3.158×10^{-1}
	$q = 0.5$	4.137×10^{-1}	3.966×10^{-1}	3.933×10^{-1}	3.931×10^{-1}	3.940×10^{-1}
	$q = 0.9$	7.959×10^{-1}	5.975×10^{-1}	5.329×10^{-1}	5.009×10^{-1}	4.821×10^{-1}

Table 5.7: Marginally-stable super-extremal Kerr-Newman-type ECO with reflective Dirichlet or Neumann boundary condition. Here we present $z_c^{\max}$ of the horizonless extremal Kerr-Newman-type ECO for different equatorial modes, $l = m$, and scalar field charge q by fixing $Q = 0.9$ and $b = 0.25$.

We observe, from Table 5.7, for a fixed equatorial mode $l = m$, the largest dimensionless critical surface radius $z_c^{\max}$ increases when we increase the scalar field charge q for both resonances conditions.

This behavior happens not only in this example but also for other values of Q. However for $Q = 0.9$ we observe two different behaviors at $z_c^{\max}$ due to the scalar field charge q. If we fix q by increasing

the equatorial modes we observe that $z_c^{\max}$ increases (valid for all values of Q). However for this example we observe that for a scalar field with $q = 0.9$ on a super-extremal Kerr-Newman-ECO with Dirichlet or Neumann boundary condition and for a scalar field with $q = 0.5$ on a super-extremal Kerr-Newman-ECO with Neumann boundary condition, $z_c^{\max}$ decreases with the equatorial modes.

Here we can also claim that the number of modes increases when we increase the equatorial modes $l = m$ or the scalar field charge q. All the results obtained are in agreement with the data obtained in [3] for $Q = 0$ and $q = 0$. Furthermore the results satisfy the upper bound (5.29).

5.3.3 Resonance spectra for near-critical approximation

In this section we present a compact resonance formula of (5.24) and (5.25) for the near-critical regime $0 < a^2 + Q^2 - 1 \ll 1$. From (5.22), we observe that $\sigma \gg l$ for this regime.

Instead of using the approximation (4.55), as we seen in Chapter 4, we will use a different approximation to the hypergeometric function for large $|b|$ where

$$ {}_2F_1(a,b;c;z) = e^{-i\pi a}\frac{\Gamma(c)}{\Gamma(c-a)}(bz)^{-a}\left[1+O\left(|bz|^{-1}\right)\right] + \frac{\Gamma(c)}{\Gamma(c)}e^{bz}(bz)^{a-c}\left[1+O\left(|bz|^{-1}\right)\right], \quad (5.32) $$

see Eq. 15.7.2 from [32]. This approximation is only applicable if $-(3\pi/2) < \mathbf{arg}(bz) < (\pi/2)$ which is our case.

Using (5.32) into (5.24) and (5.25) and changing $x \to z$, see (4.7) and (4.21) respectively, we obtain two discrete sets $\{z_c^{\mathrm{D}}(a,Q,q,l,m;n)_{n=1}^{n=N_d}\}$ and $\{z_c^{\mathrm{N}}(a,Q,q,l,m;n)_{n=1}^{n=N_n}\}$, where we have a compact formula for the former

$$ z_c^{\mathrm{D}} = -i\sqrt{a^2+Q^2-1} - \frac{\sqrt{a^2+Q^2-1}\,(1+\delta-2\sigma)}{2qQ\,\mathbf{ProductLog}\left[\frac{e^{\frac{\pi}{4qQ}(4n+\delta-1)+\frac{\mathbf{arg}\left[\Gamma\left(\frac{1}{2}(1+\delta+2iqQ)\right)\right]}{qQ}}}{2qQ}\right]}, \quad (5.33) $$

and for the latter

$$ z_c^{\mathrm{N}} = -i\sqrt{a^2+Q^2-1} - \frac{\sqrt{a^2+Q^2-1}\,(1+\delta-2\sigma)}{2qQ\,\mathbf{ProductLog}\left[\frac{e^{\frac{\pi}{4qQ}(4n+\delta-3)+\frac{\mathbf{arg}\left[\Gamma\left(\frac{1}{2}(1+\delta+2iqQ)\right)\right]}{qQ}}}{2qQ}\right]}, \quad (5.34) $$

with $n \in \mathbb{N}$. Note that these resonances equations have terms with imaginary factors. However they are so small that can be neglected.

In Table (5.8) we present the resonance spectra of the super-extremal Kerr-Newman-type in the near-critical regime for $b = 10^{-2}$, $Q = 0.1$ and $l = m = 1$. Here we compare the exact dimensionless surface radius by evaluating (5.24) and (5.25), for the variable z, with the approximated dimensionless surface radius, given by (5.33) and (5.34), respectively. Also a relative error was obtained. Here we present the absolute values of (5.33) and (5.34).

Dirichlet		$z_c\,(n=1)$	$z_c\,(n=2)$	$z_c\,(n=3)$	$z_c\,(n=4)$	$z_c\,(n=5)$
$q=0.1$	A	2.101×10^{-1}	1.262×10^{-1}	9.036×10^{-2}	7.053×10^{-2}	5.798×10^{-2}
	N	2.244×10^{-1}	1.302×10^{-1}	9.204×10^{-2}	7.114×10^{-2}	5.790×10^{-2}
	$E\,(\%)$	6.390	3.102	1.820	8.459×10^{-1}	1.334×10^{-1}
$q=0.5$	A	2.221×10^{-1}	1.329×10^{-1}	9.491×10^{-2}	7.395×10^{-2}	6.070×10^{-2}
	N	2.373×10^{-1}	1.371×10^{-1}	9.669×10^{-2}	7.464×10^{-2}	6.070×10^{-2}
	$E\,(\%)$	6.433	3.103	1.848	9.236×10^{-1}	1.110×10^{-1}
$q=0.9$	A	2.345×10^{-1}	1.397×10^{-1}	9.956×10^{-2}	7.743×10^{-2}	6.346×10^{-2}
	N	2.507×10^{-1}	1.442×10^{-1}	1.016×10^{-1}	7.820×10^{-2}	6.355×10^{-2}
	$E\,(\%)$	6.483	3.105	1.870	9.892×10^{-1}	1.355×10^{-1}

Neumann		$z_c\,(n=1)$	$z_c\,(n=2)$	$z_c\,(n=3)$	$z_c\,(n=4)$	$z_c\,(n=5)$
$q=0.1$	A	3.151×10^{-1}	1.576×10^{-1}	1.053×10^{-1}	7.920×10^{-2}	6.362×10^{-2}
	N	3.681×10^{-1}	1.647×10^{-1}	1.079×10^{-1}	8.026×10^{-2}	6.385×10^{-2}
	$E\,(\%)$	14.37	4.277	2.394	1.327	3.664×10^{-1}
$q=0.5$	A	3.340×10^{-1}	1.663×10^{-1}	1.107×10^{-1}	8.310×10^{-2}	6.665×10^{-2}
	N	3.906×10^{-1}	1.737×10^{-1}	1.134×10^{-1}	8.426×10^{-2}	6.697×10^{-2}
	$E\,(\%)$	14.50	4.276	2.403	1.377	4.751×10^{-1}
$q=0.9$	A	3.536×10^{-1}	1.751×10^{-1}	1.163×10^{-1}	8.709×10^{-2}	6.973×10^{-2}
	N	4.142×10^{-1}	1.830×10^{-1}	1.191×10^{-1}	8.834×10^{-2}	7.013×10^{-2}
	$E\,(\%)$	14.63	4.278	2.408	1.417	5.678×10^{-1}

Table 5.8: Near-critical super-extremal Kerr-Newman-type ECOs with reflective Dirichlet or Neumann boundary conditions. Here we compare the approximated radius z_c (analytical - A) with the exact radius solution (numerical - N) of the super-extremal Kerr-Newman-type ECO by calculating the relative error, E (in %). Here we set $b=10^{-2}$, $Q=0.5$ and $l=m=1$ by changing the scalar field charge q.

From Table 5.8 we observe that the dimensionless surface radius z_c decreases when we increase n for all values of q, as expected. Also when we increase n we have a better agreement between the numerical and analytical dimensionless surface radius z_c. This can be observed by the relative error, where for both reflective boundary conditions, it decreases when we increase n.

In a final remark, let us observe (5.33) and (5.34). If we approximate these equations, assuming again $\sigma \gg l$, we will obtain the same approximation (5.20) and (5.21) for the extremal case in the small-z regime. So we can conclude that the super-extremal Kerr-Newman-type ECO that supports static (marginally-stable) charged scalar field configurations when $a^2+Q^2\to 1$ starts to behave like the extremal case that we obtained in the last section.

Chapter 6

Conclusion

In this dissertation we studied a simple toy model as an alternative to BHs. The model describes an ECO that is characterized by the Kerr-Newman metric up to the vicinity of the Kerr-Newman horizon. Instead of having a horizon, however, the ECO has a surface wherein reflective boundary conditions are imposed. By considering a spherically symmetric reflective ECO and a real scalar field, one may prove that such ECO shares the same no-hair theorem as BHs; however we demonstrated that for a complex scalar field with a harmonic time dependence this ECO can support scalar field configurations.

By following the works of [1–3] we studied the ECO (in)stability when subjected to scalar field perturbations. We computed a family of critical (marginally-stable) Kerr-Newman-type ECOs, for both electrically uncharged and charged massless scalar fields. The largest of such ECOs marks the boundary between stable and unstable horizonless Kerr-Newman-type ECOs, under superradiance. We presented the existence of a discrete set of critical surface radii for three different regimes: the sub-extremal regime, the extremal regime and the super-extremal regime. The extremal Kerr-type ECO study was performed for the first time in the literature (to the best of our knowledge). These ECOs can support spatially regular static (marginally-stable) scalar field configurations.

From the results obtained, for both scalar fields, we observed the existence of two discrete sets of critical surface radius that correspond to ECOs characterized by Dirichlet or Neumann boundary conditions and we show that these discrete sets are dependent on the physical parameters $\{a, Q, q, l, m\}$ in all three regimes (for the uncharged scalar field we set $q = 0$). We gave special attention to the outermost surface critical radius, $r_c^{\max}$, due to the fact that for $r_c < r_c^{\max}$ the Kerr-Newman-type ECO suffers from superradiant instabilities whereas for $r_c > r_c^{\max}$ the Kerr-Newman-type ECO is stable.

One important goal that we could accomplish was to establish a connection between the three regimes. Globally, we can conclude that for an ECO with an electrical charge Q, regardless of q vanishing or not, $r_c^{\max}$ increases when $a \leq \sqrt{1-Q^2}$; however when $a > \sqrt{1-Q^2}$, it decreases to the point that we could have very compact ECO with $r_c = M$. Also we observed that the number of resonance solutions is infinite, in the first case, starting to decrease, in the last condition, making possible to count by hand. However there is an exception for this behavior. If we have a charged scalar field with $q = 0.9$ on a Kerr-Newman-type ECO with $Q = 0.9$, characterized by the Neumann boundary condition, we observed that $r_c^{\max}$ always increases if we increase the ECO spin a.

By changing the equatorial modes $l = m$ for a specific Kerr-Newman-ECO we also found some behaviors deviating from the trend. Typically when we increase $l = m$ the surface radius $r_c^{\max}$ increases. However if we consider higher values for both charges Q and q we observe that $r_c^{\max}$ decreases with the equatorial modes. We have also obtained compact resonance conditions through approximations, and the values are in good agreement with the numerical solutions.

At last we studied the ergoregion instability for the sub-extremal regime in the uncharged scalar field. We showed that the ergoregion radius, $r_e\,(\pi/2)$ is always above from $r_c^{\max}$, indicating that the superradiant instabilities in ECOs with $r_c < r_c^{\max}$ require that the scalar field probes the ergoregion.

In a future work we hope to explore this unique family of critical (marginally-stable) ECOs on the Kerr-Newman spacetime for massive and charged scalar fields in all three regimes.

Bibliography

[1] Shahar Hod. Onset of superradiant instabilities in rotating spacetimes of exotic compact objects. *JHEP*, 06:132, 2017.

[2] Elisa Maggio, Paolo Pani, and Valeria Ferrari. Exotic Compact Objects and How to Quench their Ergoregion Instability. *Phys. Rev.*, D96(10):104047, 2017.

[3] Shahar Hod. Ultra-spinning exotic compact objects supporting static massless scalar field configurations. *Phys. Lett.*, B774:582, 2017.

[4] Shahar Hod. No-scalar-hair theorem for spherically symmetric reflecting stars. *Phys. Rev.*, D94(10):104073, 2016.

[5] J. Michell. On the Means of Discovering the Distance, Magnitude, & c. of the Fixed Stars, in Consequence of the Diminution of the Velocity of Their Light, in Case Such a Diminution Should be Found to Take Place in any of Them, and Such Other Data Should be Procured from Observations, as Would be Farther Necessary for That Purpose. By the Rev. John Michell, B. D. F. R. S. In a Letter to Henry Cavendish, Esq. F. R. S. and A. S. *Philosophical Transactions of the Royal Society of London Series I*, 74:35–57, 1784.

[6] A. Einstein. Die Feldgleichungen der Gravitation. *Sitzungsberichte der Königlich Preußischen Akademie der Wissenschaften (Berlin), Seite 844-847.*, 1915.

[7] K. Schwarzschild. Über das Gravitationsfeld eines Massenpunktes nach der Einsteinschen Theorie. *Sitzungsberichte der Königlich Preußischen Akademie der Wissenschaften (Berlin), 1916, Seite 189-196*, 1916.

[8] R. Narayan and J. E. McClintock. Observational Evidence for Black Holes. *ArXiv e-prints*, 2013.

[9] B. P. Abbott et al. Observation of Gravitational Waves from a Binary Black Hole Merger. *Phys. Rev. Lett.*, 116(6):061102, 2016.

[10] B. P. Abbott et al. GW151226: Observation of Gravitational Waves from a 22-Solar-Mass Binary Black Hole Coalescence. *Phys. Rev. Lett.*, 116(24):241103, 2016.

[11] Benjamin P. Abbott et al. GW170104: Observation of a 50-Solar-Mass Binary Black Hole Coalescence at Redshift 0.2. *Phys. Rev. Lett.*, 118(22):221101, 2017.

[12] B. P. Abbott, R. Abbott, T. D. Abbott, F. Acernese, K. Ackley, C. Adams, T. Adams, P. Addesso, R. X. Adhikari, V. B. Adya, and et al. GW170817: Observation of Gravitational Waves from a Binary Neutron Star Inspiral. *Physical Review Letters*, 119(16):161101, October 2017.

[13] Valeri P Frolov and Andrei Zelnikov. *Introduction to black hole physics*. Oxford Univ. Press, Oxford, 2011.

[14] Piotr T. Chrusciel, Joao Lopes Costa, and Markus Heusler. Stationary Black Holes: Uniqueness and Beyond. *Living Rev. Rel.*, 15:7, 2012.

[15] N. D. Birrell and P. C. W. Davies. *Quantum Fields in Curved Space*. Cambridge Monographs on Mathematical Physics. Cambridge Univ. Press, Cambridge, UK, 1984.

[16] S. W. Hawking. Particle creation by black holes. *Communications in Mathematical Physics*,

43:199–220, August 1975.

[17] James M. Bardeen, B. Carter, and S. W. Hawking. The Four laws of black hole mechanics. *Commun. Math. Phys.*, 31:161–170, 1973.

[18] Jacob D. Bekenstein. Black holes and entropy. *Phys. Rev.*, D7:2333–2346, 1973.

[19] S. W. Hawking. Breakdown of Predictability in Gravitational Collapse. *Phys. Rev.*, D14:2460–2473, 1976.

[20] E T. Newman, R. Couch, K. Chinnapared, A. Exton, A. Prakash, and R. Torrence. Metric of a Rotating, Charged Mass. *J. Math. Phys.*, 6:918–919, 1965.

[21] Tim Adamo and E. T. Newman. The Kerr-Newman metric: A Review. *Scholarpedia*, 9:31791, 2014.

[22] Derek Raine and Edwin Thomas. *Black holes: an introduction*. World Scientific, 2005.

[23] H. Reissner. Über die Eigengravitation des elektrischen Feldes nach der Einsteinschen Theorie. *Annalen der Physik*, 355:106–120, 1916.

[24] G. Nordström. On the Energy of the Gravitation field in Einstein's Theory. *Koninklijke Nederlandse Akademie van Wetenschappen Proceedings Series B Physical Sciences*, 20:1238–1245, 1918.

[25] P. K. Townsend. Black Holes. *ArXiv General Relativity and Quantum Cosmology e-prints*, 1997.

[26] R. P. Kerr. Gravitational Field of a Spinning Mass as an Example of Algebraically Special Metrics. *Phys. Rev. Lett.*, 11:237–238, 1963.

[27] R. Penrose. Gravitational Collapse: the Role of General Relativity. *Nuovo Cimento Rivista Serie*, 1, 1969.

[28] George David Birkhoff and Rudolph Ernest Langer. *Relativity and modern physics*, volume 1. Harvard University Press Cambridge, 1923.

[29] Werner Israel. Event horizons in static vacuum space-times. *Phys. Rev.*, 164:1776–1779, 1967.

[30] B. Carter. Axisymmetric Black Hole Has Only Two Degrees of Freedom. *Phys. Rev. Lett.*, 26:331–333, 1971.

[31] D. C. Robinson. Uniqueness of the Kerr black hole. *Phys. Rev. Lett.*, 34:905, 1975.

[32] Milton Abramowitz, Irene A Stegun, et al. *Handbook of mathematical functions with formulas, graphs, and mathematical tables*, volume 9. Dover, New York, 1972.

[33] A. A. Starobinskiĭ. Amplification of waves during reflection from a rotating "black hole". *Soviet Journal of Experimental and Theoretical Physics*, 37:28, July 1973.

[34] Shahar Hod. Stationary Scalar Clouds Around Rotating Black Holes. *Phys. Rev.*, D86:104026, 2012. [Erratum: Phys. Rev.D86,129902(2012)].

[35] Carolina L. Benone, Luís C. B. Crispino, Carlos Herdeiro, and Eugen Radu. Kerr-Newman scalar clouds. *Phys. Rev.*, D90(10):104024, 2014.

[36] Elisa Maggio Matricola. Exotic compact objects as black hole mimickers: spectroscopy and stability of wormholes. Master's thesis, Facultà di Scienze Matematiche Fisiche e Naturali, 2016.

[37] Jose P. S. Lemos and Oleg B. Zaslavskii. Black hole mimickers: Regular versus singular behavior. *Phys. Rev.*, D78:024040, 2008.

[38] Zachary Mark, Aaron Zimmerman, Song Ming Du, and Yanbei Chen. A recipe for echoes from exotic compact objects. *Phys. Rev.*, D96(8):084002, 2017.

[39] P. O. Mazur and E. Mottola. Gravitational Condensate Stars: An Alternative to Black Holes. *ArXiv General Relativity and Quantum Cosmology e-prints*, 2001.

[40] Samir D. Mathur. The Fuzzball proposal for black holes: An Elementary review. *Fortsch. Phys.*, 53:793–827, 2005.

[41] David J. Kaup. Klein-Gordon Geon. *Phys. Rev.*, 172:1331–1342, 1968.

[42] Remo Ruffini and Silvano Bonazzola. Systems of selfgravitating particles in general relativity and the concept of an equation of state. *Phys. Rev.*, 187:1767–1783, 1969.

[43] Richard Brito, Vitor Cardoso, Carlos A. R. Herdeiro, and Eugen Radu. Proca stars: Gravitating Bose-Einstein condensates of massive spin-1 particles. *Phys. Lett.*, B752:291–295, 2016.

[44] F. E. Schunck and E. W. Mielke. General relativistic boson stars. *Class. Quant. Grav.*, 20:R301–R356, 2003.

[45] Steven L. Liebling and Carlos Palenzuela. Dynamical Boson Stars. *Living Rev. Rel.*, 15:6, 2012.

[46] Srijit Bhattacharjee and Sudipta Sarkar. No-hair theorems for a static and stationary reflecting star. *Phys. Rev.*, D95(8):084027, 2017.

[47] Shahar Hod. No nonminimally coupled massless scalar hair for spherically symmetric neutral reflecting stars. *Phys. Rev. D*, 96:024019, 2017.

[48] Shahar Hod. No hair for spherically symmetric neutral reflecting stars: Nonminimally coupled massive scalar fields. *Physics Letters B*, 2017.

[49] H. Weyl. Feld und Materie. *Annalen der Physik*, 370:541–563, 1921.

[50] Carlos A. R. Herdeiro and Eugen Radu. Asymptotically flat black holes with scalar hair: a review. *Int. J. Mod. Phys.*, D24(09):1542014, 2015.